Ablation of a solid by an immersed jet

Antoine Avrit, Alexandre Lecoanet, Nathalie Seiler, Nicolas Rimbert, Michel Gradeck

To cite this version:

Antoine Avrit, Alexandre Lecoanet, Nathalie Seiler, Nicolas Rimbert, Michel Gradeck. Ablation of a solid by an immersed jet. Nuclear Engineering and Design, 2023, 414, pp.112590. 10.1016/j.nucengdes.2023.112590 . hal-04410623

Highlights

Ablation of a solid by an immersed jet

Antoine Avrit, Alexandre Lecoanet, Nathalie Seiler, Nicolas Rimbert, Michel Gradeck

- New correlation on Nusselt at immersed jet impingement with melting.
- A pseudo-parabolic cavity shape, stable with time for low depths.
- Apparition of a shoulder in the cavity shape, linked to boundary layer separation.
- Local Nusselt number along the cavity characterized from the cavity shape evolution.

Ablation of a solid by an immersed jet

Antoine Avrit[a,b], Alexandre Lecoanet[a], Nathalie Seiler[a,*], Nicolas Rimbert[b], Michel Gradeck[b]

[a] *CEA, DES, IRESNE, DTN, SMTA, LMAG, Cadarache, F-13108, Saint-Paul-lez-Durance, France*
[b] *Université de Lorraine, CNRS, LEMTA, F-54000, Nancy, France*

Abstract

Issues related to the occurrence of a severe accident with melting of the core are considered as early as in the design phase of nuclear reactors. For sodium cooled fast reactors (SFR-Na), two mitigation devices are set up in the reactor vessel. The first one is "transfer tubes" that are used to relocate the corium in the lower part of the vessel; these tubes are arranged in the fuel assembly. The second one is called "core-catcher" and is supposed to receive the corium melt in the lower part of the reactor vessel. This device must absolutely be correctly designed to resist to the thermal ablation which undoubtedly will occur since the corium melt temperature is very high. In this context, experimental studies are carried out to fully understand the ablation process with simulating fluids, the final goal being to accurately simulate it in realistic conditions. Thus, an experimental study of a simplified situation is exposed using simulating materials: the core-catcher material is replaced by transparent ice and corium by a hot water jet. In this paper, the ablation of an ice block by an immersed water jet is investigated. Experiments were performed with an initial nozzle-to-solid distance $H/D_j = 10$ and the Reynolds number ranged between $\sim 10^4$ and $\sim 1.5 \times 10^5$. First, heat transfer is characterized at the stagnation point by analyzing pictures taken during cavity formation. In a second step, the cavity shape evolution is deeply analyzed to get more information about heat transfer in the whole cavity. These results help understanding the complex mechanisms at play during ablation and will be used to validate numerical simulations.

Keywords: Thermal ablation, Heat transfer, Cavity shape, Immersed jet, Nuclear safety, Sodium Fast Reactor

---

1. Introduction

This experimental study supports the safety demonstration of Sodium Fast Reactors SFR severe accident mitigation features; this kind of reactor belonging to fourth generation. In order to inhibit potential power excursion in SFR core in the case of an hypothetical severe accident, mitigation devices are introduced into the core. More specifically, they are "transfer tubes" which relocate the core molten material (called "corium") towards the bottom of the core, on a recuperator plate called core-catcher [1]. However, these devices – which effectively reduce the probability of reactivity excursions in the core – accentuate the issue of core-catcher resistance to corium inflow. Indeed, on the contrary of past core reactor design, in the case of a hypothetical accident, the presence of these transfer tubes leads to coherent corium jets in the lower plenum, from the strongback to the core-catcher [4] (fig. 1).

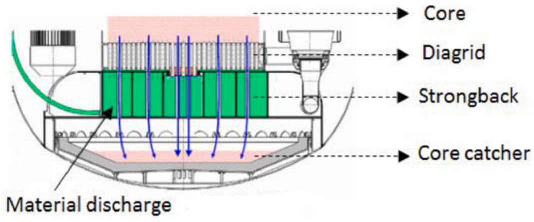

Figure 1: Cross-section of the cold pool of a SFR and sketch of the corium discharge through the transfer tubes [4].

Depending on the course of the accident, the cold sodium in the lower plenum could be vaporized, inducing pressure rises and corium jet break-up and fragmentation. Also, the thermal erosion (called ablation) of the refractory core-catcher (often in zircone or in steel) highly depends on the corium composition and temperature ($\sim$ 3000K). The core-catcher, which is another mitigation device, must be designed in such a way as to ensure that it will not lose its integrity. From this perspective, Lecoanet *et al.* [19] have studied the impact possibilities of the corium on the core-catcher and concluded that the impact of a coherent hot free-surface steel jet on a steel core-catcher is the most jeopardizing case.

In the past, studies on the thermal ablation of a solid by a jet have been made in order to characterize the maximum ablated depth. Sato *et al.* [36] studied the ablation of a metallic plate by a metallic free-surface liquid jet, showing that the velocity of ablation remains constant as long as the cavity does not fill with the jet liquid. Gilpin [12] studied the ablation of an ice block by a free-surface water jet, and studied the evolution of the stagnation Nusselt number versus the Reynolds number of the jet. Lecoanet *et al.* [20, 19] studied the same problem, and characterized several ablation regimes depending on several dimensionless parameters of the jet. They also studied the "pool-effect", characterized by a reduction of the ablation rate when the cavity is filled with liquid. More recently, Tromm and Gauss-Liu [45] performed large-scale jet impingement tests with prototypical reactor conditions (steel jet) on a metallic core catcher. The experiments demonstrated

---

[*] Corresponding author. E-mail address: nathalie.seiler@cea.fr

Nomenclature

Dimensionless numbers

$B \equiv \frac{c_{p,j}(T_j - T_m)}{L + c_{p,s}(T_m - T_{-\infty})}$ Melting number

$Nu \equiv \frac{hD_j}{\lambda_j}$ Nusselt number

$Pr_j \equiv \frac{\nu}{\alpha_{th,j}}$ Jet Prandtl number

$Re_j \equiv \frac{D_j V_j}{\nu}$ Jet Reynolds number

Notations

D	Diameter (m)
H	Initial nozzle-to-solid distance (m)
h	Convective heat transfer coefficient (W/m^2/K)
r	Radial coordinate (m)
t	Time (s)
U, V	Velocity (m/s)
y	Depth of the cavity (m)
z	Axial distance from the nozzle exit (m)

Physical properties

α_{th}	Thermal diffusivity (m^2/s)
λ	Thermal conductivity (W/m/K)
μ	Dynamic viscosity (kg/m/s)
ν	Kinematic viscosity (m^2/s)
ρ	Density (kg/m^3)
c_p	Specific heat (J/kg/K)
L	Latent heat (J/kg)

Subscripts

j	Refers to the jet at the nozzle exit
m	Refers to the melting phenomenon
ref	Refers to the a reference quantity
s	Refers to the solid
w	Refers to the impinged surface
$-\infty$	Refers to the solid far from the liquid-solid interface
0	Refers to the stagnation point
∞	Refers to the surrounding fluid
c	Refers to a quantity evaluated at the jet center ($r = 0$)

that the pool effect leads to reduced ablation rate (compared to the case where the cavity is not filled with liquid); the Nusselt number has been measured and found to be in good agreement with the predictions of the early study by Sato *et al.* [36]. These experiments are very valuable at a macroscopic scale but do not allow us to understand the local physical phenomena governing heat transfer and melting.

With this final goal in mind, a R & D methodology is followed in this study based on a simplified situation using simulating materials, which enable visualization. In this paper, the ablation of an ice block by an immersed water jet is investigated. This case – performed with simulating material – allows to investigate the local physics and is not completely uncorrelated with the real reactor case, as demonstrated by [20, 19] which compared the dimensionless numbers of interest for this physical issue.

So, in addition to investigating experimentally the local physics of a water jet impacting on an ice block, CFD simulations are carried out and validated on experimental results. Once the simulation methodology has been validated (meshing, turbulence models, etc.), CFD simulations of steel jets on a steel block will be carried out. Li *et al.* [24, 23] studied numerically the ablation by a free-surface jet with the reactor case material, using a particle method, showing an ablation dynamic quite different from what was observed for the water-ice case.

Starting with the simplest case to understand ablation phenomenology and validate simulations, the purpose of this work is to characterize the thermal ablation in the case of an immersed jet. Regarding the safety issue, this case is another limiting case, when corium is already on the core-catcher or when the pool-effect is reached.

This paper first presents a review of the phenomenology of immersed jets impingement: the hydrodynamics and heat exchanges without and with phase change. Then, in section 3.1, the experimental device and tests are presented before analyzing and interpreting the main results in terms of heat transfer at the jet stagnation point (in section 4) and farther downstream (in section 5), leading to various cavity shapes. A correlation of the Nusselt at the jet stagnation, whose form was established from past studies evidence, is derived from these experimental results, since no correlation for an immersed jet with melting is available in the literature.

2. Phenomenology of impinging round immersed heated jets

In this section the main past works and findings on immersed hot jets impingement and related heat and mass transfers are summarized; this includes the main outcomes on hydrodynamics and heat transfers, first without wall melting and then with phase change at the wall.

2.1. Hydrodynamics of a round impinging jet

3 flow regions, illustrated in Figure 2, are usually considered when studying a turbulent immersed impinging jet [11, 35]:

a. The "free jet" region: this region is located upstream of the impinged surface and is not affected by the presence of this surface. The characteristics of this free jet region have been widely studied, and solutions for the Reynolds-averaged equations have been brought by Tollmien [44] and Görtler [15] depending on the way Reynolds' stresses are modeled. Two sub-regions can be distinguished depending on the distance to the nozzle: close to the nozzle is a flow region called the "potential core" where the velocity at the center of the jet remains constant. Further from the nozzle, the flow is developing, the turbulence reaches the center of the jet and the centerline velocity $U_c = U(r = 0, z)$ decreases with the distance from the nozzle z ($z = 0$ at the nozzle exit). The separation between these two sub-regions happens for $z/D_j \sim 5 - 6$ [17, 11, 46]. For $z/D_j > 6$, the temperature at the center of the jet tends towards the surrounding fluid's temperature and the velocity at the center decreases as $1/z$ [34, 35, 3]. The temperature follows a similar behavior according to Bejan [3]: $(T(r = 0, z) - T_\infty) \propto 1/z$ where T_∞ is the temperature of the surrounding fluid.

b. The "stagnation" region, downstream of the previous region and located around the stagnation point (or impingement point at the jet axis $r = 0$ and $z = H$ where H is the distance between the nozzle and the solid): the direction of flow changes due to the influence of the wall, leading to a high pressure around the stagnation point. In this region, the boundary layer has an almost constant thickness [46, 31]. Tani and Komasu [42] have studied experimentally the flow in this region and obtained several velocity profiles and pressure profiles at the wall. They noticed that in a sub-region such that $r \lesssim D_j$ there was almost no viscous dissipation in the flow. The vertical extensions of the stagnation region is estimated around $2D_j$ and its radial extension around $4D_j$ (for $r < 2D_j$) by Tani and Komasu [42]. For $H/D_j > 6$, a "developed" free jet impinges the solid, leading to an increase of the turbulence intensity (comparing the magnitude of the fluctuations to the magnitude of the velocity of the mean flow) due to the mixing with the surrounding fluid. These turbulent fluctuations lead to an increase of the transfers (heat and mass) at the wall, by disturbing the boundary layer.

c. The "wall jet" region, downstream of the stagnation region. An analytical study was carried by Glauert [13] for laminar and turbulent flows in the "wall jet" region: the flow in this region can be divided into two layers depending on the distance to the wall. In the "inner" layer (very close to the wall), the flow can be described by the equations of a boundary layer, whereas in the "outer" layer (farther from the wall), the flow is close to a mixing-layer flow. The separation between those two layers occurs when the velocity reaches its maximum (the point of maximum velocity depends on Re_j). To obtain a solution for the turbulent flow, Glauert uses an empirical formula on the wall shear-stress for the boundary layer equations and a turbulent viscosity hypothesis along with a mixing-length hypothesis for the outer layer equations. His analytical solution for the velocity was compared with experimental results from Bakke [2] and Sigalla [38] and showed good agreement.

2.2. Heat transfer at the wall

Heat transfers between a round immersed jet and a wall normal to the jet axis have been extensively studied in the literature. The heat transfer between a solid and a fluid are usually characterized by the Nusselt number Nu and the convective heat transfer coefficient h, defined by:

$$h = \frac{\lambda_s}{T_w - T_{ref}} \left.\frac{\partial T}{\partial n}\right|_w \tag{1}$$

$$Nu = \frac{hD_j}{\lambda_j} \tag{2}$$

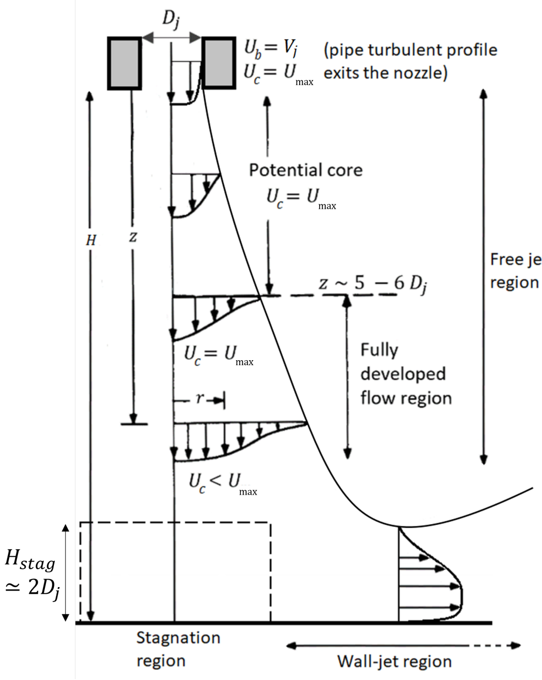

Figure 2: Illustration of the flow for an immersed impinging jet. U_b stands for "bulk velocity", U_c stands for "centerline velocity", and U_{max} is the maximum of the pipe turbulent velocity profile.

Where λ_j denotes the jet fluid thermal conductivity, the subscript w denotes a variable evaluated at the impinged surface (or wall) and T_{ref} is a reference temperature for the considered problem, for example the surrounding fluid temperature T_∞.

Depending on the value of H/D_j (dimensionless nozzle-to-solid distance), it is either the jet potential core flow ($H/D_j < 6$) or the developed jet flow ($H/D_j > 6$) that impinges the solid. For $H/D_j < 6$, the highest value for Nu is not located at the stagnation point due to the fact that the turbulence intensity is lower at the jet center (the turbulence created by the mixing with the surrounding fluid has not reached the center of the jet for $H/D_j \lesssim 5 - 6$) [46]. If $H/D_j > 6$, the free jet flow is fully developed when it impinges and the maximum of Nu is located at the stagnation point: $\max\left(Nu(r)\right) = Nu(r = 0) = Nu_0$.

For immersed impinging jets without melting, Nu_0 has been characterized extensively depending on the jet parameters, expressed in terms of two dimensionless numbers:

- the Reynolds number of the jet $Re_j = \frac{D_j V_j}{\nu_j}$ where ν_j is the cinematic viscosity of the jet evaluated at the nozzle exit.
- the Prandtl number of the jet $Pr_j = \frac{\alpha_{th,j}}{\nu_j}$ where $\alpha_{th,j}$ is the thermal diffusivity of the jet evaluated at the nozzle exit.

For a given value of H/D_j, most authors obtained a correlation for the Nusselt number at the stagnation point, Nu_0, depending on Re_j and Pr_j as:

$$Nu_0 \;=\; C_{H/D_j}\; Re_j^{\alpha}\; Pr_j^{\beta} \tag{3}$$

Where C_{H/D_j} is a function of H/D_j only, α is the exponent associated to Re_j and β to Pr_j. The previous form is usual for correlations in forced convection [37]. In the case of an impinging jet without melting of the solid, the value of β is usually set between 0.3 and 0.42 according to several authors [39, 6, 27] and Webb and Ma [47] obtained the value of 0.42 for water.

An analysis for a fully laminar flow in the stagnation region's boundary layer gives $\alpha = \frac{1}{2}$ according to Liu *et al.* [27] and Webb and Ma [47]. This value seems to remain valid for an impinging potential core ($H/D_j < 5 - 6$) even if the jet is turbulent [46]. However, for larger values of H/D_j, there seems to be no agreement in the literature about the value of α. Livingood and Hrycak [28] reported values ranging from ~ 0.5 to ~ 0.8 and Chamberlain [5] obtained a value of ~ 0.56. Lee [22] gives $Nu \propto Re_j^{0.65}$ for $H/D_j > 6$ and $5000 < Re_j < 70000$; previous studies agree that the exponent on Re_j is higher when $H/D_j > 6$ than for $H/D_j < 5 - 6$. No correlation could be found for $Re_j > 70000$ and $H/D_j > 6$; however, a value close to 0.8, which is the exponent obtained for a turbulent boundary layer on a flat plate [26], can be expected for $Re_j > 10^5$ and $H/D_j > 6$.

Those results were obtained for jets impinging solids without melting. The effect of the melting of the solid is investigated in the next paragraph.

2.3. Impinging round jet with melting

For a free-surface jet (a liquid jet in a gaseous atmosphere) impinging a solid with melting (if the molten solid and the liquid are of the same type), an enthalpy balance at the melting surface gives the following relation according to Sato *et al.* [36]:

$$h\left(T_{ref} - T_m\right) = V_m \rho_s \left[L + c_{p,s}\left(T_m - T_{s,-\infty}\right)\right] \tag{4}$$

Where T_{ref} is a reference temperature, $T_{s,-\infty}$ is the temperature of the solid far from the solid-liquid interface and V_m is the velocity of the solid-fluid interface due to the melting, also called "velocity of ablation".

From equation 4, a new equation can be derived involving a new dimensionless number B called the "melting number":

$$\rho_s V_m = \frac{h}{c_{p,j}} B \tag{5}$$

with

$$B = \frac{c_{p,j}(T_j - T_m)}{L + c_{p,s}(T_m - T_{s,init})} \tag{6}$$

This dimensionless number compares the energy brought by the jet to the energy necessary to bring the solid to its melting temperature and melt it.

It is possible to link Nu and V_m using Eq. (5) and the definition of the Nusselt number in Eq. (2):

$$Nu = \frac{\rho_s D_j c_{p,j} V_m}{B \lambda_j} \tag{7}$$

At the stagnation point, $V_m = V_{m,0}$ is simply defined as the derivative of the depth of the cavity y_0 with respect to time t:

$$V_{m,0} = \frac{\mathrm{d}y_0}{\mathrm{d}t} \tag{8}$$

Thus, for a melting surface, the heat transfer at the impingement point can simply be studied by screening the evolution of cavity depth with time.

No data is available on the heat transfer for an immersed jet impinging a melting solid. However, it seems reasonable to assume that equation (4), established for a free-surface jet remain valid in case of an immersed jet. Indeed, the thermal balance proposed by Sato *et al.* [36] only depends on the reference temperature considered in the left part of the equation, which could be taken as the jet temperature T_j.

Moreover, several authors have studied heat transfers between a fluid and solid with melting for other problems. Machicoane *et al.* [30] studied the melting of ice balls in a turbulent flow, and established:

$$Nu \propto Re^{0.8} \tag{9}$$

Epstein [8] established a relation between the Nusselt number Nu^{nm} obtained between a fluid and a non-melting solid (nm here stands for "non-melting"), the Nusselt number Nu^{m} obtained between the same fluid and solid when the melting phenomenon is added and the melting number B as follows:

$$\frac{Nu^m}{Nu^{nm}} = \frac{\log(1+B)}{B} \tag{10}$$

This previous relation was established for a laminar flow over a melting solid. According to Tien and Yen [43], this relation is also valid for turbulent flows over a melting solid. This relation could thus be used to transpose the results obtained for turbulent immersed impinging jets without melting to the ablation by a turbulent immersed jet: this method has already been applied to the case of the ablation of a solid by a free-surface jet with success [20].

Considering Equation (3) and the previous relation (10), a correlation of the following form is expected for the case of an impinging immersed jet with melting of the solid:

$$Nu_0 = \mathcal{C}_{y_0/D_j} \, Re_j^{\alpha} \, Pr_j^{\beta} \, \frac{\log(1+B)}{B} \tag{11}$$

With $\mathcal{C}_{y_0/D_j}$ a function of y_0/D_j and potentially H/D_j (the dependence on H/D_j could not be assessed in experiments where H does not vary). Based on the result given by Machicoane *et al.* [30] and the exponents given on Re for the impinging jet without melting (with the transposition proposed by Epstein [8] through Equation (10)), the exponent α on Re_j is expected to be in the range $0.65 - 0.8$.

The purpose of this experimental work is to establish a correlation in the form of the one established from past studies evidences (eq. (11)) to predict the maximum heat transfer (at the stagnation point) based on the jet parameters, since no correlation for an immersed jet with melting is available in the literature. Thus, the ablation of an ice block by an immersed water jet is experimentally investigated in the next section leading to the characterization of the heat transfers between the solid and the liquid during the ablation at the impinging point but also farther downstream. The cavity shape and the evolution of the heat transfer with r are also studied.

3. Experimental studies

3.1. Experimental apparatus

The experimental apparatus is called Hot Ablation of a SOlid by a Liquid - Observation (*HAnSoLO*). It is well described in [20] [18]. This experimental setup allowed to visualize the ablation phenomenon induced by a heated free surface liquid jet, impinging a transparent ice block. In this experimental facility, water is heated in a tank with an immersed heater, then flows through a screw pump, a three way valve and finally through a heated nozzle to impact an ice block. The velocity and temperature of the jet are controlled with a flowmeter and several thermocouples. The ice block is made such that the ice is transparent (the process to obtain a block of high quality is detailed by Lecoanet *et al.* [20]) ; a high-speed camera allows the visualization of the ablation of the ice by the hot jet.

A recent adaptation of the *HAnSoLO* apparatus now allows to perform experiments of ablation by an immersed water jet. This adaptation is summarized in this article and a simplified vision of the modified installation is given in Figure 3a. The ice block and the nozzle are now immersed in a tank filled with initially cold water. The temperature of this water is set at $T_{w,init} = 277 \pm 1$ K (however the water is not cooled throughout the experiment). The tank is transparent so that it is still possible to visualize the cavity during the experiments and use the high-speed camera to film it.

An example of picture obtained with the camera is given in Figure 3b. The free surface between the room's air and the surrounding water can be seen, as well as the immersed nozzle and the thermocouples used to control the temperature of the ice before the impingement. The thermocouple measuring the surrounding water's temperature cannot be seen in this picture.

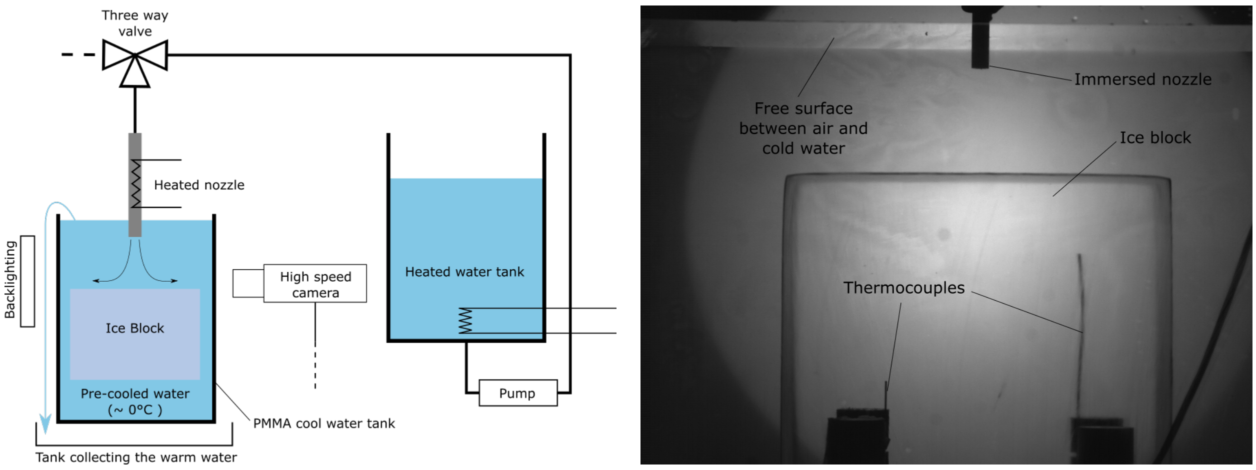

(a) *HAnSoLO* for immersed jets.

(b) Picture from the high-speed camera.

Figure 3: (a) Schematic of the modified *HAnSoLO* apparatus for immersed jets; (b) Example of a picture taken by the high speed camera with additional information.

3.2. Experimental parameters

The ranges of dimensionless numbers available with *HAnSoLO* are given in Table 1. According to the range of Re_j, the jets are turbulent [25] ($Re_j > 4000$ for all experiments), which is also the case for the reactor case. The ranges expected in the reactor case [18] are also given in Table 1 for comparison. In both cases, the jet material and the molten material are identical. Re_j is lower for the experiments performed with HAnSoLO than in the reactor case, however the dependence of the heat transfers to Re_j is expected to remain the same in both cases since the jets are fully turbulent. The ranges of B are almost identical in both cases which should lead to similar ablation regimes. In the reactor case, $Pr_j < 1$ whereas $Pr_j > 1$ in the *HAnSoLO* experiments, thus there is no similarity in terms of Pr_j: this is why a CFD code should be validated (with the present experiments) and used to simulate the reactor case, in a future work.

Although there is no similarity in terms of Pr_j, experiments of ablation by a free surface jet carried out for water and ice [19] and for liquid and solid stainless steel [45] showed good agreement [18, 21]. Thus, the experimental results obtained in this study could enable an approximate prediction the ablation by an immersed jet in the reactor configuration.

	HAnSoLO	Reactor case
Re_j	$1.2 \times 10^4 \;-\; 1.5 \times 10^5$	$\sim 10^6$
Pr_j	$2.5 \;-\; 5.5$	$\sim 0.1 \;-\; 0.6$
B	$0.3 \;-\; 0.9$	$\sim 0.25 \;-\; 0.95$

Table 1: Ranges of dimensionless numbers.

Those numbers are obtained with jet temperatures T_j ranging between 303K and 343K, and jet velocity V_j ranging between $1.0\text{m}\cdot\text{s}^{-1}$ and $10\text{m}\cdot\text{s}^{-1}$. Pr_j varies only with T_j, and Re_j varies with both V_j and T_j. The evolution of Re and Pr with the temperature is given in Appendix A.

Tests are performed with constant H (the initial distance between the nozzle and the ice block) and a constant jet diameter D_j. The value of H/D_j is set to 10, thus a developed jet impinges the solid (the turbulence has reached the jet center). A round nozzle is used, with an internal diameter of $D_j =$ 6mm ± 0.1mm. A tube longer than $50D_j$ is set upstream of the nozzle in order to ensure that the velocity profile is a fully developed turbulent profile at the exit [25]. Five different velocities V_j are considered: $V_j \in \{1.0,\ 2.5,\ 5,\ 7.5,\ 10\}\text{m}\cdot\text{s}^{-1}$, as well as three different temperatures $T_j \in \{303,\ 323,\ 343\}$ K. 12 different experiments are discussed in this article. The experiments are represented in a Pr_j versus Re_j diagram in Figure 4 in order to show their values and their uncertainties during the experimental campaign.

During each experiment, the flow rate and the temperature at the nozzle are measured continuously (allowing the evaluation of the uncertainties on the dimensionless numbers). The frame rate of the high speed camera is set to 50 images per second. The temperature of the ice blocks is measured during the experiments and is always close to the melting temperature. Before the experiments, the ice blocks are stored at $T_{s,-\infty} \simeq 268\text{K}$. Hence, the initial temperature of the ice varies between 268K and 273K (~ 268K at the center of the block and up to 273K at the edge of the block).

According to Lecoanet *et al.* [20], it is possible to evaluate the influence of the non-uniform temperature distribution inside the ice block (between $T_{s,-\infty}$ and T_m) with the Stefan number St which is written as:

$$St = \frac{c_{p,s}(T_m - T_{s,-\infty})}{L}$$

This number compares the energy necessary to heat a certain volume up to its melting temperature with the energy necessary to melt this volume of ice. In the experiments $St \sim 10^{-2}$, hence the non-uniform

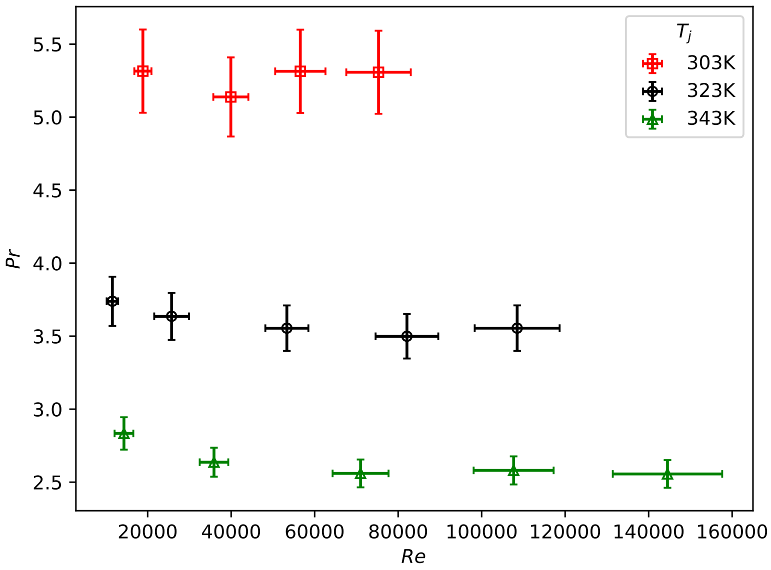

Figure 4: Representation of the experiments based on their Prandtl and Reynolds numbers evaluated at the nozzle exit.

distribution of temperature should have little influence on the dynamic of the ablation [20] in the present case.

The temperature of the water in which the nozzle and the ice block are immersed is also measured at the beginning of the experiments, and is around $T^{water} = 277 \pm 1\text{K}$. The melting of the ice block by the cold surrounding water can be neglected compared to the melting induced by the hot jet: the melting due to the diffusion of heat by the surrounding water (before impingement of the jet) is much slower than the melting by the convection due to the jet. The characteristic times associated are:

$$\tau_{diff,melt} \sim \frac{D_j^2}{\alpha} \frac{L}{c_{p,f}(T_\infty - T_m)} \quad \text{and} \quad \tau_{conv,melt} \sim \frac{D_j L}{V_j c_{p,f}(T_j - T_m)}$$

Using the minimum jet velocity $V_j = 1.0\text{m}\cdot\text{s}^{-1}$ and the minimum jet temperature $T_j = 303\text{K}$, we obtain:

$$\begin{cases} \tau_{diff,melt} & \sim & 644\text{s} \\ \tau_{conv,melt} & \sim & 0.01\text{s} \end{cases}$$

Since $\tau_{diff,melt} >> \tau_{conv,melt}$, the melting by diffusion from the surrounding fluid can be neglected compared to the melting due to the jet.

4. Heat transfer at the stagnation point

The experiments are performed for $H/D_j = 10 > 6$ [35], leading to a maximum ablation at the stagnation point. The characterization of the maximum ablation is important for the reactor case in order to dimension the core-catcher. In future studies, CFD simulations will help to check whether the correlation that will be established here for water will remain valid in steel. The characterization of the maximum ablation can be done by computing the depth of the cavity at the stagnation point, which allows to evaluate the heat transfer at this location: the procedures used for this purpose are described in the following paragraph.

4.1. Procedure to obtain the depth at the stagnation point

During an experiment, the high-speed camera saves a visualization of the ice block and of the jet every 0.02s. A few seconds after the jet has impinged the ice block, the block starts to melt due to the heat transfer from the jet. A cavity appears, which grows with time. The evolution of the cavity can be followed through the images of the high-speed camera. An example of several images obtained by the camera for an experiment performed with $V_j = 5\,\text{m}\cdot\text{s}^{-1}$ ($Re_j \sim 5.3 \times 10^4$) and $T_j = 323\text{K}$ ($Pr_j = 3.58$ and $B = 0.61$) is shown in Figure 5. The images have a resolution of 1024×1024 px^2. The pixel to centimeter conversion ranges between 25 and 30 (pixels for one centimeter), depending on the experiments (the camera can be moved between experiments, leading to a variable distance the camera and the ice block).

A frequency of 50 images per second is enough to correctly describe the evolution of the cavity: Lecoanet *et al.* [20] obtained values of $V_{m,0}$ up to $8.82 \times 10^{-3}\,\text{m}\cdot\text{s}^{-1}$ for a free-surface water jet impinging an ice block, with the same range of Re_j as in the present experiments. Between two images (every 0.02s), the displacement of the cavity is up to $0.02 \cdot 8.82 \times 10^{-3} \simeq 1.7 \times 10^{-4}\text{m}$; in the present experiments, $V_{m,0}$ is expected to be lower than in the experiments of Lecoanet *et al.* [20] due to the dissipation of the jet energy in the surrounding fluid, leading to a displacement of the interface smaller than the previous computed value. The distance between two pixel centers in the present experiments is between $1/(30 \times 10^2) \simeq 3.3 \times 10^{-4}\text{m}$ and $1/(25 \times 10^2) = 4.0 \times 10^{-4}\text{m}$ (based on the pixel to centimeter conversion rates given previously). This means that the solid-liquid interface cannot move through more than one pixel between two pictures, leading to a good time resolution for the evolution of the cavity.

The growth of the cavity can be observed on those pictures. On images 5b and 5c, bubbles can be observed, emitted from the nozzle. They are created by air trapped in the circuit upstream from the nozzle

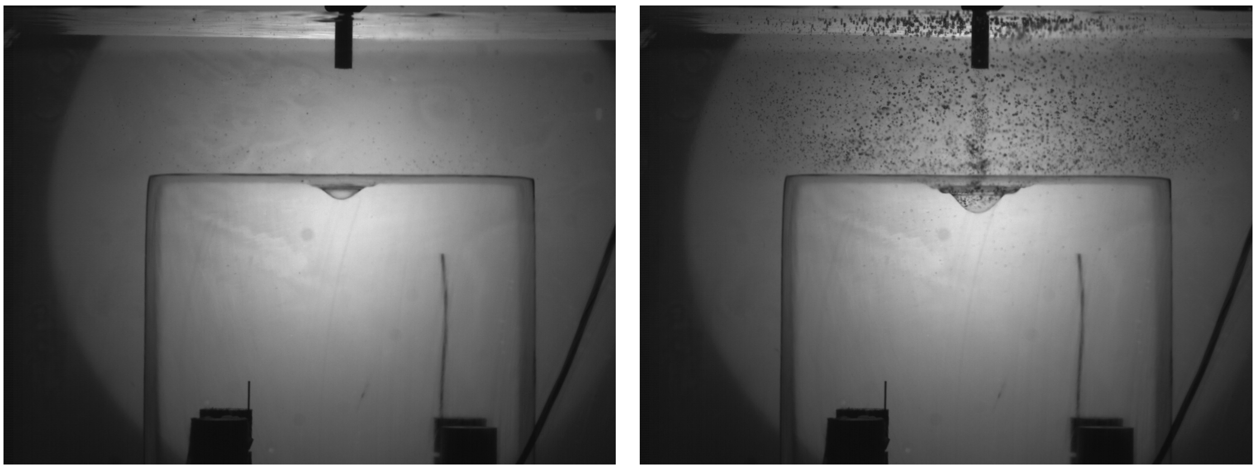

(a) Cavity at $t = 5s$. (b) Cavity at $t = 9s$.

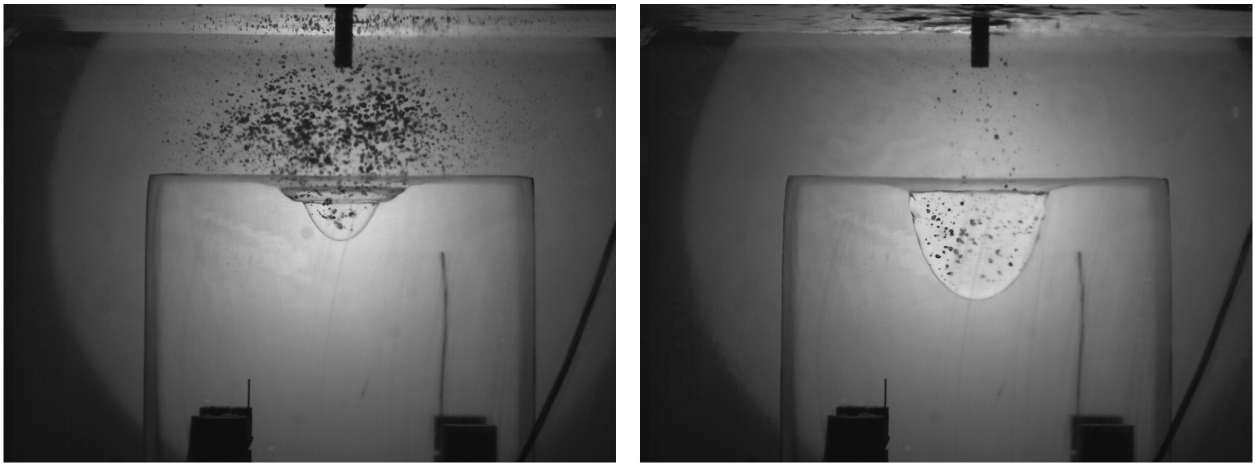

(c) Cavity at $t = 20s$. (d) Cavity at $t = 50s$.

Figure 5: Evolution of the cavity through time as recorded by the high-speed camera. The experiment is performed with $V_j = 5\,\mathrm{m \cdot s^{-1}}$ ($Re_j \sim 5.3 \times 10^4$) and $T_j = 323\mathrm{K}$.

exit. The effect of those bubbles on the ablation is neglectible in this analysis, due to the fact that the volume fraction of the bubbles is low in the jet; in most experiments no bubble appear.

An image treatment algorithm is used in order to compute the depth of the cavity at the stagnation point and the cavity shape, using the images recorded by the camera. The algorithms are based on those developed by Lecoanet [18, 19]: the interface detection method relies on the high contrast of the liquid-solid interface. Pictures are converted into float arrays with values ranging from 0 to 255 (pictures are in black and white, thus one byte is enough to characterize each pixel). The arrays associated to 20 consecutive images are averaged (with a moving average in order to keep a high time resolution) in order to reduce the noise from one image to the following. A threshold is applied to the values (0 - 255) of the resulting array to convert the values into booleans: if the value is higher than the threshold, it is converted into 1, otherwise into 0. The threshold is generally taken between 10 and 30 depending on the contrast of the images. This procedure allows to detect the areas in the picture where the luminosity changes, hence highlighting areas of high contrast.

This method allows to detect the interface using its contrast but also detects the bubbles since they also present a high contrast (see Figure 5). A procedure is thus used to remove bubbles, by removing small objects: an object is defined as a set of pixels having a given value (in the boolean array, 0 or 1), and having at least one pixel of the same boolean value in their vicinity (at the left, right, top or bottom). If the number of pixels of the object is lower than a certain threshold, the object is removed by setting the value of these pixels to the opposite (in terms of booleans). The usual value of the threshold used for this procedure is 100 pixels minimum for an object not to be removed.

The depth at the stagnation point y_0 (where y is the local depth of the cavity and the subscript 0 refers to the stagnation point) can be computed with this procedure, by searching for the high contrast area in the jet axis.

The characterization of the heat transfer at the stagnation point is done by computing the Nusselt number Nu_0 at the stagnation point.

The depth at the stagnation point y_0 can be directly linked to the ablation velocity $V_{m,0}$ at this point (the velocity of the interface, defined in Equation (8)) and then to Nu_0, with relation (7), which leads to the following relation:

$$Nu_0 \;=\; \frac{\rho_s D_j c_{p,j}}{B\lambda_j}\, V_m \;=\; \frac{\rho_s D_j c_{p,j}}{B\lambda_j}\,\frac{dy_0}{dt} \tag{12}$$

For $V_j = 5\,\mathrm{m \cdot s^{-1}}$ ($Re_j \sim 5.3 \times 10^4$) and $T_j = 323\mathrm{K}$, the curves of y_0/D_j and Nu_0 with respect to time are given in Figure 6. The curve of y_0/D_j versus t directly computed by the image treatment algorithm is represented in Figure 6a as a solid black line with the label "Original curve".

The "original curve" of y_0/D_j versus t in Figure 6a shows nonphysical oscillations and asperities (artificially created during the image-processing), which results in major oscillations when applying the time derivative to the curve. Filtering operations are necessary to obtain $V_{m,0}$ and Nu_0 versus time from $\frac{dy_0}{dt}$, in

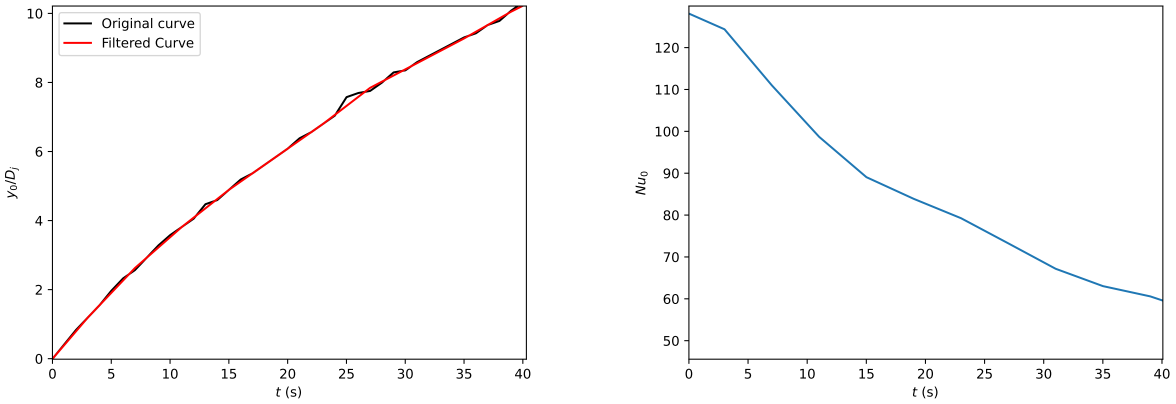

(a) y_0/D_j versus t.

(b) Nu_0 versus t.

Figure 6: a) Evolution of the dimensionless depth of the cavity at the stagnation point y_0/D_j during the ablation; b) Evolution of the Nusselt number at the stagnation point Nu_0 during the ablation. The experiment is performed with $V_j = 5\,\mathrm{m\cdot s^{-1}}$ ($Re_j \sim 5.3 \times 10^4$) and $T_j = 323$K.

order to delete that effect. Hence, a first order filter and a moving average are applied to the curve y_0/D_j versus t before computing $V_{m,0}$ and Nu_0.

As observed in Figure 6a, the filtered curve of y_0/D_j versus t (red solid line labeled "Filtered curve") is very close to the original curve, but does not show the nonphysical behavior previously identified. The resulting curve of Nu_0 plotted in Figure 6b does not show numerical oscillations.

As observed in Figure 6a, y_0/D_j increases monotonously with t, but the local slope of the curve decreases through time: as y_0/D_j increases, the free jet flow reaches the stagnation region with less energy because of the increasing distance between the stagnation point and the nozzle exit. As a result, Nu_0 decreases monotonously with t, as shown on Figure 6b. This behavior is observed for all values of Re_j and Pr_j considered in the experiments; this is the main difference with the free-surface jet experiments for which Nu remains constant as long as the cavity is not filled with liquid [20, 36].

In order to compare the values of Nu_0 between the experiments, the evolution of Nu_0 versus y_0/D_j is considered (for a given value of t, the values of Nu_0 and y_0 are known, and both functions are bijective with respect to time); this allows to compare the values obtained for Nu_0 depending on the jet parameters at a given ablated depth, rather than at a given time.

The uncertainties on the jet parameters and on the computed Nusselt numbers are determined with the methodology given in Appendix B.

4.2. Characterization of the heat transfer at the stagnation point

The purpose of this analysis is to characterize the heat transfer at the stagnation point, by finding a global correlation between Nu_0 and all the dimensionless numbers of the problem (using the results of all experiments shown in Figure 4). The correlation is sought as :

$$Nu_0 \;=\; \mathcal{C}_{y_0/D_j} \cdot f_1(Re_j) \cdot f_2(Pr_j) \cdot f_3(B) \tag{13}$$

Based on Equation (11), the following forms are expected for f_1, f_2 and f_3:

$$\left\{ \begin{array}{rcl} f_1(Re_j) & = & Re_j^{\alpha} \\ f_2(Pr_j) & = & Pr_j^{\beta} \\ f_3(B) & = & \frac{\log(1+B)}{B} \end{array} \right. \tag{14}$$

with α and β two constants (supposed independent of y_0/D_j and of the jet parameters), that will be computed from the experimental points. The chosen characteristics of α, β and $\mathcal{C}_{y_0/D_j}$ allow to isolate the effect of each parameter on Nu_0.

4.2.1. Exponent on Re_j

Methodology and results of the analysis. To study the dependence of Nu_0 to Re_j only, the experiments are treated separately for each value of T_j (303, 323 or 343K), so that Pr_j and B do not vary. The purpose is to determine the exponent α in Equation (14). The methodology is the following:

- For each experiment performed at a given T_j, the curve of Nu_0 versus y_0/D_j is computed.
- At a given value of y_0/D_j, the corresponding value of Nu_0 is associated to the value of Re_j for each experiment, leading to a curve of Nu_0 versus Re_j.
- A linear regression is computed on $\log Nu_0$ versus $\log Re_j$ to determine the value of α. This relies on the fact that T_j and y_0/D_j are fixed, so that:

$$\log Nu_0 \;=\; \alpha \log Re_j + \underbrace{\log\left(\mathcal{C}_{y_0/D_j} \cdot f_2(Pr_j) \cdot f_3(B)\right)}_{=\ constant}$$

α is computed as the slope of the linear regression.

- The previous steps are repeated for 50 linearly spaced values of y_0/D_j in order to determine the evolution of α with y_0/D_j. The average value of α is the value retained for the considered T_j, since α was assumed to be independent of y_0/D_j.

The previous methodology applied for each T_j leads to the following values:

$$\begin{cases} \alpha(T_j = 303\text{K}) \simeq 0.682 \ \pm \ 0.070 \\ \alpha(T_j = 323\text{K}) \simeq 0.636 \ \pm \ 0.034 \\ \alpha(T_j = 343\text{K}) \simeq 0.624 \ \pm \ 0.028 \end{cases} \tag{15}$$

The average value obtained for each temperature is within the range predicted by the literature [22, 30, 28]. The method to compute the uncertainty on α is described in Appendix B.

This approximation of α being constant when y_0/D_j varies seems reasonable for all values of T_j as shown in Figures 7b and 7a (respectively for $T_j = 303$K and $T_j = 323$K): the value of α oscillates around the average value when y_0/D_j varies. The evolution of α for $T_j = 343$K is very close to the evolution shown in Figure 7b for $T_j = 323$K, thus the curve is not shown here for concision.

The value of α used in the global correlation is here chosen as the value averaged on all temperatures (α was assumed to be independent of the jet parameters, which seems to be a reasonable hypothesis based on the results), leading to $\alpha \simeq 0.65 \pm 0.07$ (the uncertainty is here taken as the maximum of the uncertainties on the $\alpha(T_j)$), which is very close to what was obtained by Lee [22].

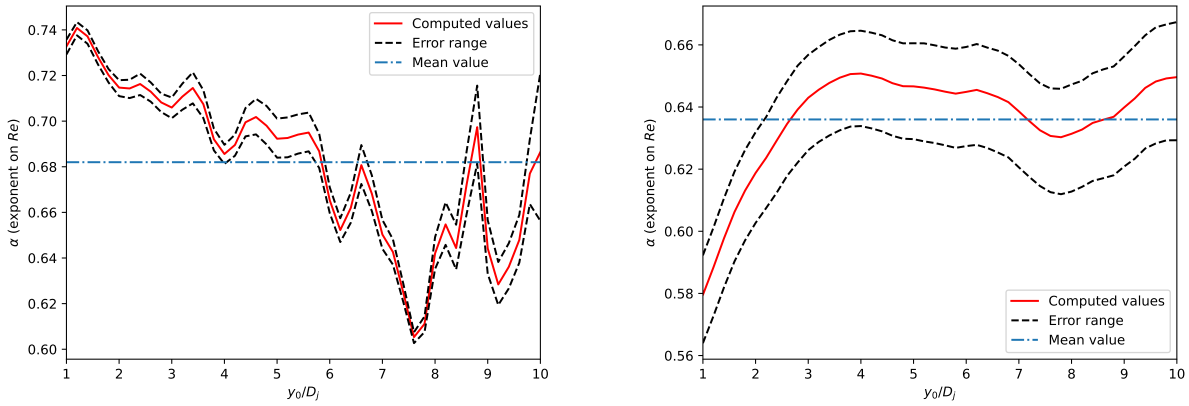

(a) α vs y_0/D_j at $T_j = 303$K.

(b) α vs y_0/D_j at $T_j = 323$K.

Figure 7: Evolution of the value of the exponent α versus y_0/D_j, for a) $T_j = 303$K; b) $T_j = 323$K. The black dashed line ($--$) represents the uncertainty range on α (see Appendix B for the methodology) and the blue dash-dotted line ($- \cdot -$) is the mean value.

The mean value $\alpha \simeq 0.65 \pm 0.07$ will be used in the global correlation.

4.2.2. Exponent on Pr_j

For a given value of y_0/D_j, the exponent β on Pr_j is determined with an iterative method.

Several values of β (100 values, linearly spaced between 0.7 and 1.0) are tested, in order to find the "optimal" value:

- For a given value of β, the experimental points Nu_0 versus $Re_j^{0.65}\ Pr_j^{\beta}\ \frac{\log(1+B)}{B}$ are computed for each experiment at the considered depth (the exponent 0.65 on Re_j comes from the previous paragraph and the form of the function applied to B was given in Equation (14)).
- A linear regression is performed on all the points computed previously.
- The error between the experimental points and the linear regression is computed.

The value of β minimizing the error is the "optimal" value for the considered depth.

This methodology is applied for several values of y_0/D_j (50 values, linearly spaced between 0 and 10) to study the evolution of the "optimal" value of β with y_0/D_j.

The resulting curve of β versus y_0/D_j is shown in Figure 8. A notable variation of β with y_0/D_j can be observed for $y_0/D_j < 4$.

This gives the following average value:

$$\beta_{av} \ \simeq \ 0.73 \tag{16}$$

where β_{av} is the value of β averaged on all depths. $\beta = \beta_{av}$ will be used in the global correlation (13) since β was assumed to be independent of y_0/D_j: this approximation seems reasonable for $y_0/D_j \gtrsim 5$, where the values obtained for β oscillate around 0.67, but it is questionable for lower values of y_0/D_j. However, the hypothesis of β being independent of y_0/D_j is kept in the global correlation (13) (in order to isolate the effect of each parameter on Nu_0).

The computed value of β is higher than what was found in the literature for immersed jets impinging non-melting surfaces (between 0.3 and 0.42). Sato *et al.* [36] performed experiments with free-surface jets of liquid metals impinging a solid plate with melting and obtained 0.8 as the value of the exponent on Pr in their correlation. The range of Pr used in their experiments was $0.0095 < Pr < 0.20$. The value obtained by these authors for a problem of jet impingement with melting of the surface is quite similar to the mean

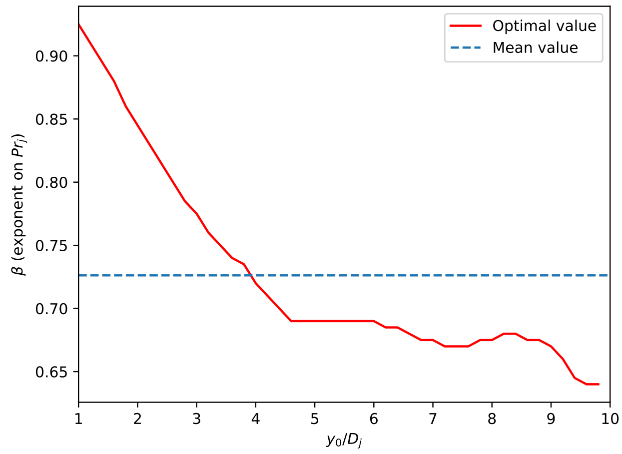

Figure 8: Exponent β on Pr versus y_0/D_j.

value β obtained here; the observed high value obtained here for β (by comparison to the non-melting case, where $0.3 < \beta < 0.42$) could thus be linked to the melting phenomenon for an immersed jet.

The uncertainty on β is taken as twice the standard deviation of β_{y_0/D_j}, thus the value $\beta = 0.73 \pm 0.15$ will be used in the global correlation.

4.2.3. Prefactor $\mathcal{C}_{y_0/D_j}$

The methodology to determine the value of $\mathcal{C}_{y_0/D_j}$ for a given value of y_0/D_j is the following:

- Nu_0 and $Re_j^{0.65}\ Pr_j^{0.73}\ \frac{\log(1+B)}{B}$ are computed at y_0/D_j for each experiment.
- Based on correlation (13), the curve of Nu_0 versus $Re_j^{0.65}\ Pr_j^{0.73}\ \frac{\log(1+B)}{B}$ should be a straight line: a linear regression is thus computed.
- The slope computed by the linear regression is the value of $\mathcal{C}_{y_0/D_j}$ at the considered depth.

An example (for visualization) is given in Figure 9 for $y_0/D_j = 5$ (the alignment of the points was also observed for other values of y_0/D_j), showing the linear regression and the corresponding experimental points (Nu_0 versus $Re_j^{0.65}\ Pr_j^{0.73}\ \frac{\log(1+B)}{B}$); this shows that the approximation of $Nu_0 \propto Re_j^{0.65}\ Pr_j^{0.73}\ \frac{\log(1+B)}{B}$ seems reasonable.

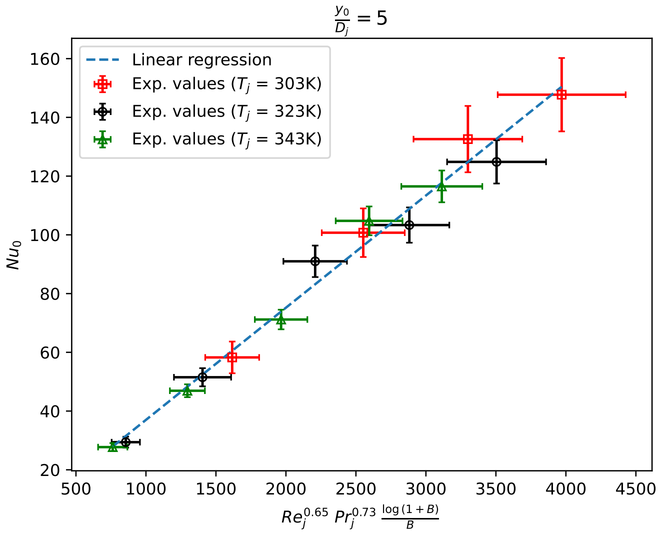

Figure 9: Nu_0 versus $Re_j^{0.65}\ Pr_j^{0.73}\ \frac{\log(1+B)}{B}$ at $y_0/D_j = 5$. The dashed curve is the corresponding linear regression curve.

Applying this methodology for several depths allows to compute $\mathcal{C}_{y_0/D_j}$ with respect to y_0/D_j: this is carried out for 50 values of y_0/D_j here (linearly spaced between 0 and 10).

Using a logarithmic scale on the y-axis gives a pseudo-linear curve for $\mathcal{C}_{y_0/D_j}$. Hence, $\mathcal{C}_{y_0/D_j}$ is sought under the form :

$$\mathcal{C}_{y_0/D_j} = b\ \exp\left(a\frac{y_0}{D_j}\right) \tag{17}$$

A linear regression applied to the logarithm of the previous equation allows to evaluate the values of a and b, giving:

$$\mathcal{C}_{y_0/D_j} = 0.054\ \exp\left(-0.0775\frac{y_0}{D_j}\right), \quad (r^2 = 0.993) \tag{18}$$

This gives a maximum gap between the regression and $\mathcal{C}_{y_0/D_j}$ of 3%. The computed curve of $\mathcal{C}_{y_0/D_j}$ and this regression are shown in Figure 10 (the regression has the label "*exp*-regression"), showing a good agreement between the regression and the computed values of $\mathcal{C}_{y_0/D_j}$.

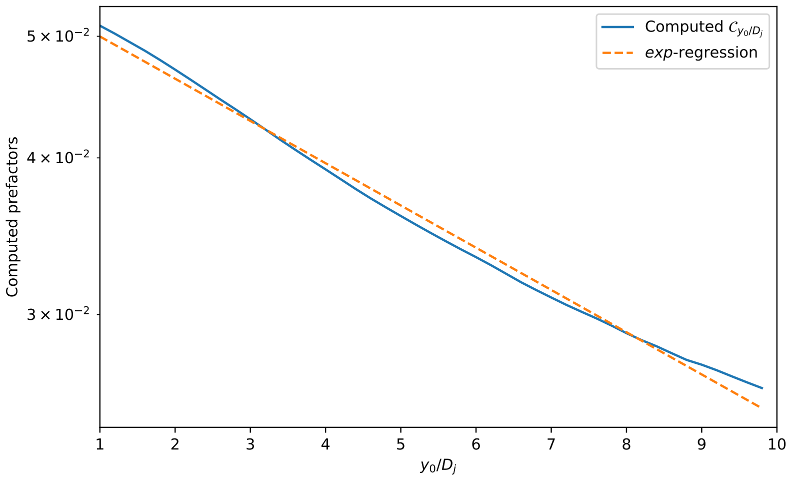

Figure 10: Evolution of the prefactor $\mathcal{C}_{y_0/D_j}$ with y_0/D_j. The dashed curve is the regression given in Equation (18).

4.2.4. Validation of the correlation

Based on the previous results, the global correlation, established for $H/D_j = 10$, given in Equation (13) can be written as:

$$Nu_0 \;=\; 0.054 \;\exp\left(-0.0775\frac{y_0}{D_j}\right)\cdot Re_j^{0.65}\cdot Pr_j^{0.73}\cdot\frac{\log\left(1+B\right)}{B} \tag{19}$$

The average of the maximum error on all experiments is 13.5%, with a minimum of 5.2% and a maximum of 29.3%. Table 2 shows the maximum error for each experiment.

Error (%) for each experiment		V_j ($\mathrm{m\cdot s^{-1}}$)				
		1.0	2.5	5.0	7.5	10.0
T_j (K)	303	/	9.0	15.3	14.8	8.4
	323	12.6	12.5	8.5	29.3	22.0
	343	7.4	5.2	23.1	13.0	8.3

Table 2: Error (in percent) between the global correlation (19) and the curves of Nu_0 computed from the experiments.

Three experiments lead to errors superior to 20%, the other errors are inferior or equal to 15.3%. This correlation gives satisfying results in order to predict Nu_0 based on Re_j, Pr_j, B and y_0/D_j.

A first characterization of the maximum heat transfer (at the stagnation point) during the ablation by an immersed jet was obtained in this section. The radial evolution of the heat transfers is studied in the next section.

5. Analysis of the cavity shape

5.1. Procedure to obtain the cavity shape

Computation of the cavity shape relies on the same method described previously (subsection 4.1); here, the whole shape is computed instead of just the stagnation point depth. Details of the initial method could be found in [18, 19]. Improvements have been made to compute Nu versus r using the cavity shape evolution (the method is described in subsection 5.4), which requires a cavity shape that has a continuous derivative.

An example of what is directly computed by the image-treatment algorithm is shown in Figure 11 as a blue line labeled "Original". Plateaus can be seen on the curve (which are caused by the resolution of the image), a plateau being defined by several consecutive points (at least 2) of identical value; those plateaus are problematic when computing the local normal to the curve which is necessary to evaluate the local Nu (see subsection 5.4). To obtain a cavity shape with a continuous curvature, the following treatment is applied to the cavity shape:

a. The cavity shape is first centered to ensure that the maximum depth is exactly located at $r/D_j = 0$.

b. An anti-aliasing operation is applied to the cavity shape: the points of a given plateau are replaced by a linear interpolation between the first point in the plateau of coordinates (r_f, y_f) and the first point out of the plateau of coordinates (r_o, y_o): the ordinate y_k of the points of coordinates (r_k, y_k) are modified by the relation:

$$y_k \;=\; y_f\cdot\frac{r_k - r_f}{r_o - r_f} + y_o\cdot\frac{r_o - r_k}{r_o - r_f} \tag{20}$$

This is done for all plateaus, and reduces the oscillations in the slope of the curve.

c. To erase possible artificial oscillations, a decimation operation is performed: only 1 point out of 4 are kept in the curve. This can be done since the initial resolution (in terms of number of points) of the curve is very important. A moving average is then applied to the curve.

d. The shapes obtained for $r/D_j < 0$ (left side of the cavity) and for $r/D_j > 0$ are averaged to ensure the axisymetric behavior.

The cavity shape after treatment is shown in Figure 11 (label "Treated"), and superimposed with the original shape. The treated shape appears smoother but remains very close to the original curve. This give a maximum error between the two shapes of 3.7%: the physical behavior is kept in the treated curve and the numerical oscillations are drastically reduced when computing the local normal to the curve.

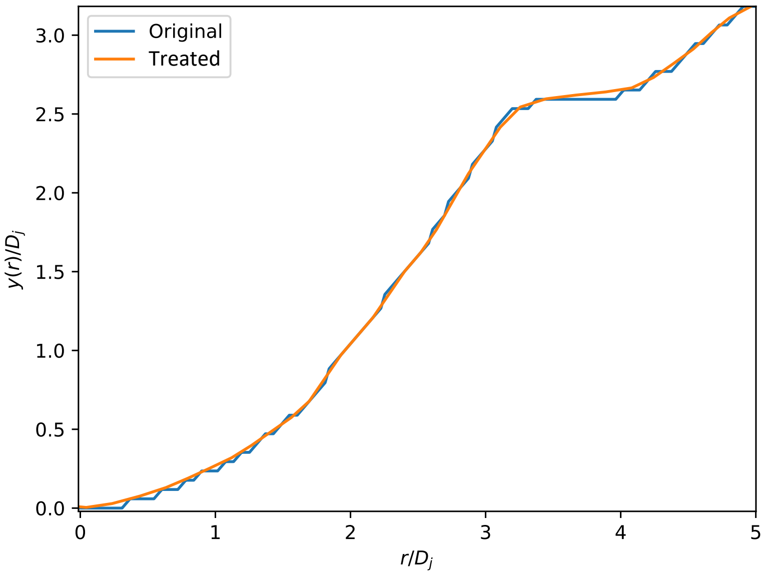

Figure 11: Comparison of the cavity shapes before ("Original") and after treatment ("Treated"). Cavity shape obtained for $V_j = 5\,\mathrm{m \cdot s^{-1}}$ ($Re_j \simeq 5.3 \times 10^4$) and $T_j = 323\mathrm{K}$, at $t \simeq 12.6\mathrm{s}$.

The analysis in the remaining section is performed for experiments at $T_j = 323\mathrm{K}$ only (but similar behavior is observed for other temperatures).

5.2. Auto-similar cavity shape

Cavity shapes obtained at different times for $V_j = 5\,\mathrm{m \cdot s^{-1}}$ and $T_j = 323\mathrm{K}$ are shown in Figure 12. Cavity shapes for $t < 12\mathrm{s}$ are not represented due to a low measurement precision when the depth of the cavity is low.

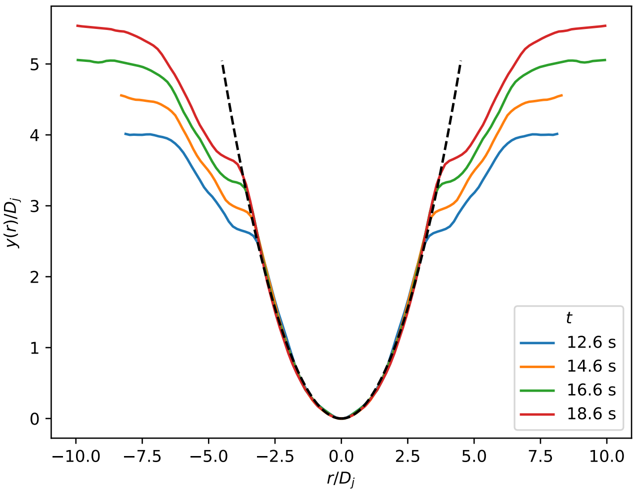

Figure 12: Cavity shapes for several times ($V_j = 5\,\mathrm{m \cdot s^{-1}}$ and $T_j = 323\mathrm{K}$). The parabolic shape computed with Equation (22) is represented as dashed black line (−−).

For $r/D_j > 3$, a "shoulder" can be observed (the shoulder corresponds to the region of rapid change of curvature between for $2.5 < r/D_j < 5$): this can follow from a local increase of the heat transfer. This increase may be linked to a boundary layer separation, created by a change of curvature of the cavity. The cavity is concave close to the stagnation point and becomes convex further (in order to make the joint between the ablated part of the ice and the surface of the block still not molten). A convex shape with important curvature can lead to boundary layer separation (Lopes *et al.* [29]). The boundary layer can also be destabilized by the melting phenomenon, which creates a velocity normal to the wall, due to the melting of the solid. The shoulder appears very early in the experiment but its appearance cannot be studied: the resolution of the pictures does not allow to study the structure of the cavity shape for $y_0/D_j < 1$.

In the region such that $|r| < 2.5D_j$, the cavity is auto-similar with respect to time: the shapes obtained for different times can be superimposed. The cavity seems to have a parabolic shape in this region. Applying a square root to $y(r)/D_j$ shows that the cavity can be approximated by a parabola: as can be seen in Figure 13, $\sqrt{y(r)/D_j}$ is quasi-linear with r. The behavior observed for values of r/D_j close to 0 is due to the low resolution in points in this area, leading to numerical artifacts.

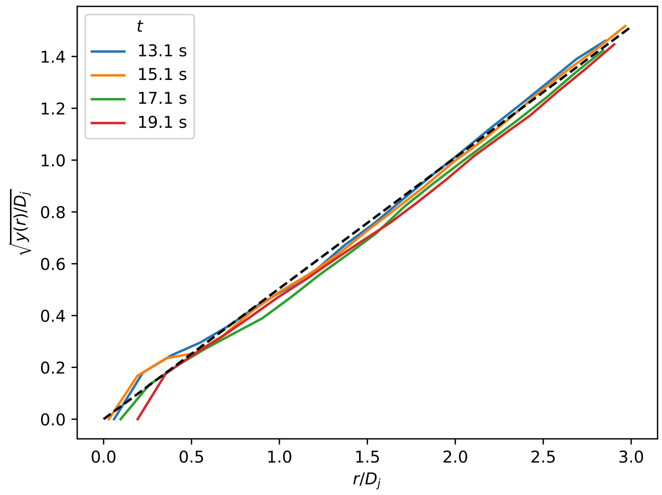

Figure 13: Square root of $y(r)/D_j$ for several times and for $0 < r/D_j < 3$ ($V_j = 5\,\mathrm{m \cdot s^{-1}}$ and $T_j = 323\mathrm{K}$, $Re_j \simeq 5.3 \times 10^4$). The dashed curve (——) is the parabolic approximation of the cavity shape (Eq. (21)).

A linear regression applied on each profile of $\sqrt{y(r)/D_j}$ leads to:

$$\sqrt{y(r)/D_j} \simeq 0.499\ r/D_j \tag{21}$$

The slope of $\sqrt{y(r)/D_j}$ with respect to r is also shown in Figure 13. For $r < 3D_j$, the cavity shape can thus be approximated by the following parabola:

$$\frac{y(r)}{D_j} \simeq 0.249 \left(\frac{r}{D_j}\right)^2 \tag{22}$$

The multiplicative coefficient in the previous equation is noted γ_p (p subscript stands for "parabola"). For several values of Re_j, the following parabolas are obtained:

$$\begin{cases} \gamma_p \simeq 0.301 & \text{for } Re_j \simeq 2.6 \times 10^4 \\ \gamma_p \simeq 0.249 & \text{for } Re_j \simeq 5.3 \times 10^4 \\ \gamma_p \simeq 0.215 & \text{for } Re_j \simeq 8.2 \times 10^4 \\ \gamma_p \simeq 0.193 & \text{for } Re_j \simeq 1.1 \times 10^5 \end{cases} \tag{23}$$

The decrease of γ_p when Re_j increases means that the cavity is wider for higher values of Re_j: the heat transfer decreases more slowly when r/D_j increases. A linear regression using previous values gives the following correlation:

$$\gamma_p \propto Re_j^{-0.31} \tag{24}$$

The evolution of γ_p versus Re_j and the correlation (24) are represented in Figure 14, and show good agreement.

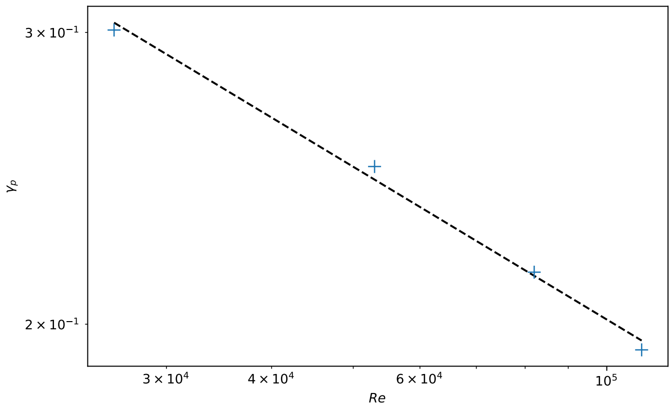

Figure 14: γ_p versus Re_j ($T_j = 323\mathrm{K}$). Blue crosses (+) correspond to the experimental values of γ_p and the correlation (Eq. (24)) is shown as a dashed line.

Swedish *et al.* [40] as well as Furutani *et al.* [10] studied the melting of a solid near the stagnation point of a free-surface jet and concluded that the molten solid forms a small layer between the jet fluid and the solid, leading to a reduction of the heat transfer. Increasing Re_j would lead to an improved removal of this layer and to a more important heat transfer all along the surface of the cavity; explaining a wider cavity when Re_j increases. A comparison of the cavity shapes for these four experiments is given in Figure 15 for $y_0/D_j = 6$.

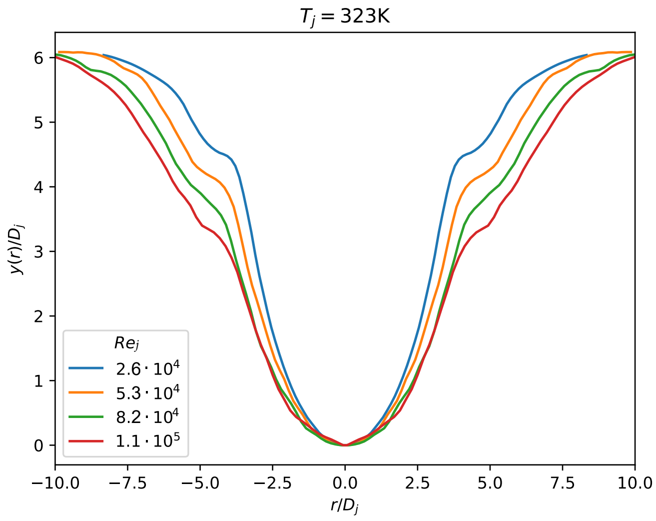

Figure 15: Comparison of the cavity shapes obtained for several values of Re_j (for $T_j = 323$K and $y_0/D_j = 6$).

5.3. Analysis of the shoulder

A boundary layer separates from a surface in the presence of an adverse pressure gradient [7, 37], and the separation point is characterized by $\tau_w = 0$ where τ_w is the wall shear-stress. The separation can be caused by the curvature of the surface: the wake behind a cylinder is a well-know example of separation of a boundary layer on a convex surface.

The parabolic part of the cavity is concave; Taghinia *et al.* [41] have studied numerically the impingement of an immersed jet on a concave surface and did not highlight a separation of the boundary layer from the wall. The cavity is convex further from the stagnation point, and, from experiments, the boundary layer separation seems to occur in this convex region.

A fit of the following form can be applied to the whole cavity for $y_0/D_j < 6$ (as long as the auto-similar approximation remains valid):

$$f(r) \;=\; \frac{y_0}{D_j}\left(1 - \exp\left[-\gamma_e\left(\frac{r}{D_j}\right)^2\right]\right) \tag{25}$$

The superposition of the cavity shape with this fit is given in Figure 16a for $Re_j = 5.3 \times 10^4$ and $T_j = 323$K, and in Figure 16b for $Re_j = 1.1 \times 10^5$ and $T_j = 323$K. The fit deviates from the cavity shape at the shoulder location, but the deviation decreases when reaching the ice block surface.

This fit has a coherent shape with the parabola found previously, close to the stagnation point:

$$1 - \exp\left(-\gamma_e x^2\right) \sim \gamma_e x^2 \;+\; o(x^2) \tag{26}$$

for $\gamma_e x^2$ close to 0. Since the separation does not happen in the concave part of the cavity, it may occur once the convex part is reached, so beyond the inflection point.

An inflection point of a function f is a point for which the sign of f'' changes. In this case:

$$f''(r) \;=\; 2\gamma_e\frac{y_0}{D_j^3}\left[1 - 2\gamma_e\left(\frac{r}{D_j}\right)^2\right] \cdot \exp\left[-\gamma_e\left(\frac{r}{D_j}\right)^2\right] \tag{27}$$

The sign of f'' changes for $r/D_j = (2\gamma_e)^{-1/2}$, leading to an inflection point that occurs at:

$$\frac{y_{infl}}{D_j} = \left[1 - \exp\left(-\frac{1}{2}\right)\right] \cdot \frac{y_0}{D_j} \simeq 0.39\frac{y_0}{D_j} \tag{28}$$

which is to say that the inflection point is located at 39% of the total height of the cavity.

In this analysis, the height (y_{infl}/D_j) of the inflection point does not depend on the value of Re_j. Figure 16 shows the superposition of the fit (Equation(25)) and of the cavity shape for $Re_j \simeq 5.3 \times 10^4$ (Figure 16a) and $Re_j \simeq 1.1 \times 10^5$ (Figure 16b). The inflection point computed from the fit (Equation(25)) is also represented. For both values of Re_j the inflection point is located upstream of the shoulder, meaning that the boundary layer does not separate from the wall immediately after reaching the inflection point (red '×' points), but separates in the convex part of the surface of the cavity.

The fact that the separation occurs systematically after the inflection point suggests that the curvature in the convex part of the cavity might be involved in the separation of the boundary layer. Re_j also has an effect on the separation: based on Figure 16, the shoulder is located closer to the stagnation point (in terms of distance along the wall) when Re_j increases.

Drozdz *et al.* [7] have studied the effect of Re_j on the separation of a boundary layer on a flat plate and concluded that the separation happens later when Re_j increases due to the increase of the wall shear stress through the turbulence; this behavior seems contradictory with what is observed in Figure 16. However, in the present study, the melting phenomenon at the wall has an effect similar to a blowing wall: the normal velocity is not zero, and as the solid melts, fluid is "injected" by the interface towards the boundary layer according to Swedish *et al.* [40]. According to several authors [49, 37, 32], a "blowing" interface - meaning an interface injecting fluid in its normal direction - tends to promote the development of a boundary layer,

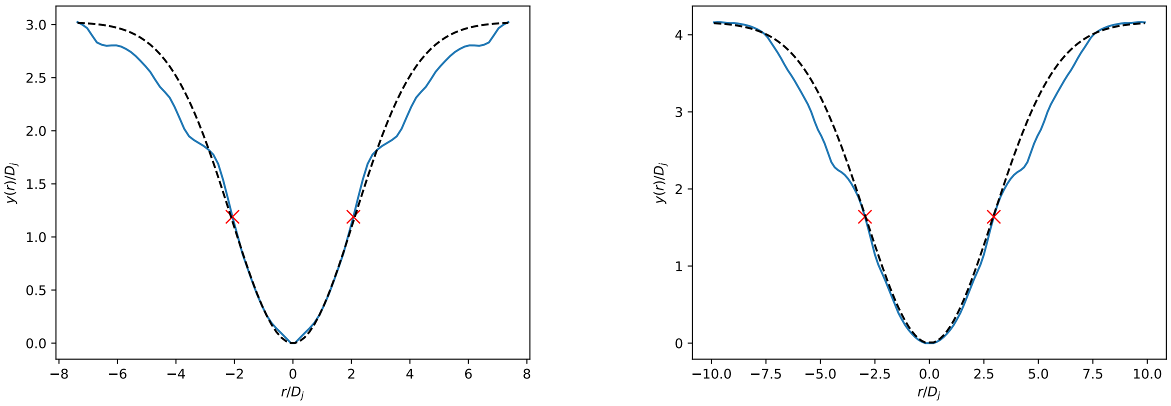

(a) Cavity shape and fit (Eq. (25)) for $Re_j = 5.3 \times 10^4$ and $T_j = 323\text{K}$.

(b) Cavity shape and fit (Eq. (25)) for $Re_j = 1.1 \times 10^5$ and $T_j = 323\text{K}$.

Figure 16: Cavity shape and fit (Eq. (25)) for: (a) $Re_j = 5.3 \times 10^4$ ($T_j = 323\text{K}$); (b) $Re_j = 1.1 \times 10^5$ ($T_j = 323\text{K}$). Red '×' points are the inflection points computed from the fit. Both cavity shapes are obtained for $y_0/D_j = 4$.

which could lead to an earlier separation compared to a case with no fluid injection: a blowing condition at the wall leads to significant decrease of the wall shear stress by thickening the boundary layer. A decrease of the wall shear stress would trigger an earlier separation of the boundary layer. Furthermore, as said previously, a higher value of Re_j could increase the convection of the molten solid layer described by Swedish *et al.* [40], resulting in a higher heat transfer and thus to a more important blowing at the wall for higher values of Re_j.

Based on these elements, an earlier (in terms of distance to the stagnation point) separation of the boundary layer could occur when increasing Re_j for a flow over a convex blowing wall.

5.4. Radial Nusselt profile

The radial profile of Nu in the cavity can be determined using the cavity shape evolution. $Nu(r)$ is linked to the local ablation velocity $V_m(r)$ by the relation (7). However, for $r \neq 0$, V_m is defined as the velocity of the solid-liquid interface in the local normal direction to this interface.

At a given time t, the cavity shape $\mathcal{S}_t$ is compared to another cavity shape at $t+\Delta t$, in order to determine the distance traveled by the interface during Δt at any r. For a given value of r, the local slope m of $\mathcal{S}_t$ is computed, in order to determine the local normal vector $\vec{n}$ with the formula $\vec{n} = \begin{pmatrix} m \\ -1 \end{pmatrix}$.

The intersection point between the normal vector and the cavity shape $\mathcal{S}_{t+\Delta t}$ is then computed, which gives the distance traveled by the interface in the normal direction.

The result of this procedure is applied to an experiment with $Re_j \sim 2.6 \times 10^4$ and $T_j = 323\text{K}$. $\Delta t = 3\text{s}$ is used (for higher values of Δt, the results do not vary), so that the space between the two cavity shapes is large enough to avoid oscillations during the numerical treatment. For t such that $y_0/D_j = 2$, the computed Nu profile for $r/D_j \in [0, 3]$ is shown in Figure 17.

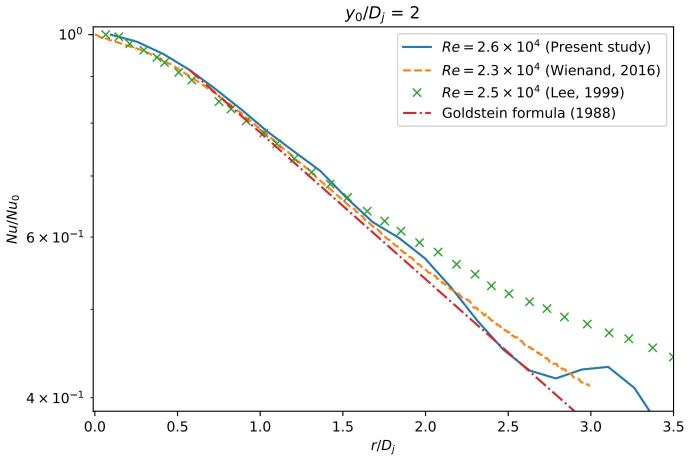

Figure 17: $\frac{Nu}{Nu_0}$ radial profile for $y_0/D_j = 2$ ($Re_j \simeq 2.6 \times 10^4$ and $T_j = 323\text{K}$). Results from the literature are also shown: Wienand *et al.* [48] (−−), Lee [22] (×) and Goldstein and Franchett [14] (− · −), obtained for jet impingement on a flat plate without melting.

The logarithmic plot on the y-axis shows that Nu decreases exponentially for $r > 0.5D_j$, but decreases very slowly close to the stagnation point.

The resulting curve is compared to several results of jet impingement **without melting** taken from the literature: Lee [22] obtained several radial profiles of Nu depending on Re_j, including one at $Re_j = 2.5 \times 10^4$ shown here; Goldstein and Franchett [14] obtained a correlation between $Nu/Re_j^{0.7}$ and r for normal and inclined impinging jets; for a normal jet, they obtained:

$$\frac{Nu}{Re_j^{0.7}} = 0.123 \, \exp\left(-0.37 \frac{r}{D_j}\right) \tag{29}$$

This correlation is shown for $r > 0.5D_j$ (the starting point is taken on the experimental curve) because the behavior is not exponential for $r < 0.5D_j$. Finally, Wienand *et al.* [48] numerically studied a jet impinging a flat plate without melting for $Re_j = 2.3 \times 10^4$ with a RANS approach and a k-ω SST model, the resulting curve is also shown on the same figure.

All those results are consistent, meaning that the melting and the curvature of the cavity do not have a high influence on the heat transfer for low depth such that $y_0/D_j \leq 2$ (the main influence is in the value of Nu_0 which is why the radial profiles of Nu are scaled by Nu_0).

The radial profile of Nu for several depths such that $y_0/D_j \geq 2$ is shown in Figure 18.

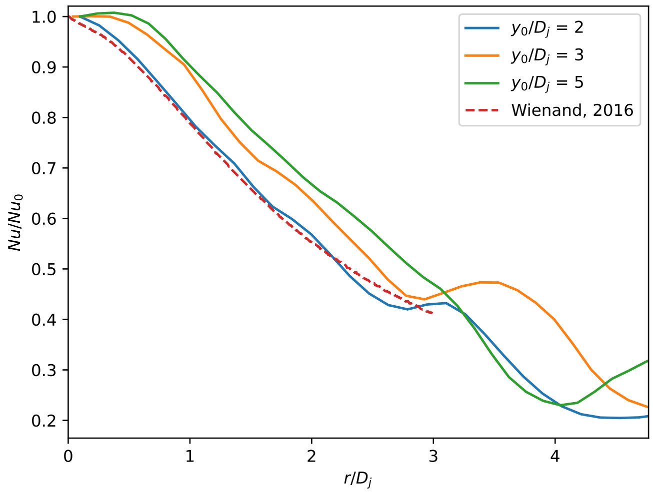

Figure 18: $\frac{Nu}{Nu_0}$ radial profile for several values of y_0/D_j ($Re_j \simeq 2.6 \times 10^4$ and $T_j = 323$K).

For $y_0/D_j > 2$, a region where $Nu \simeq Nu_0$ remains close to the stagnation point. A local maximum of Nu appears further from the stagnation point, which corresponds to the shoulder mentioned previously. This local maximum moves away from the stagnation point as the cavity grows. As y_0/D_j increases, the radial profile of Nu deviates from the profile given by Wienand *et al.* [48] (shown in Figures 17 and 18), meaning the effect of the cavity's shape and the effect of the surface melting become more significant as y_0/D_j increases.

The effect of the cavity's shape can be understood as follows: the fluid brought by the jet upstream can get "trapped" in the cavity due to re-circulations, because of the shape of the cavity. This leads to an increase of $\frac{Nu(r)}{Nu_0}$ with y_0/D_j once the cavity is deep enough: the fluid exchanges more of its heat with the solid before getting out of the cavity.

6. Conclusions

Following the introduction in SFR-type reactors of new means of mitigating reactivity insertions, in the hypothetical event of a severe accident, molten core material would be relocated directly to the core catcher via mitigation tubes directly connecting the core to the core-catcher. In this case, very hot jets of molten material could coherently impact the core-catcher and lead to its very rapid thermal erosion (ablation). In this context, while macroscopic tests of free steel jet on steel solid are carried out elsewhere [45], it was decided to pursue a different R & D study methodology on a local scale in order to investigate the phenomenology. The problem of the ablation by an immersed jet was considered; it is a limiting case without fragmentation of the jet. The ablation of an ice block by an immersed water jet was investigated, allowing local visualization and measurement. Experiments are performed with an initial nozzle-to-solid distance equal to 10 jet diameters and the Reynolds number ranged between 10^4 and 1.5×10^5; the representativity of these study parameters to the reactor problem have been discussed here and in [19]. Free surface jet ablation experiments conducted for different materials [19, 45, 21] suggest that the experimental results obtained in the present paper could predict the immersed jet ablation in the reactor configuration.

The results of these experimental tests enabled to carry out a local analysis of the ablation phenomenology, investigating the origin of the shape of the cavity obtained, which features a shoulder. Particular attention was paid to heat transfer at the point of impact, which is maximum in the case of a submerged jet with a nozzle-to-solid distance greater than 6 jet diameters. Heat transfer was characterized at the stagnation point by analyzing pictures taken during cavity formation. In order to obtain a useful correlation for zero-dimensional severe accident simulation tools, the form of the relation between the Nusselt number and other non-dimensional number has been derived from a literature review of past works on jet impingement and the value of the involved variables determined from experimental results. This work has enabled to establish the first correlation of heat transfer at the impact of an immersed jet on a melting solid of the same material.

In a second step, the cavity shape evolution is deeply analyzed to get a deeper understanding of local phenomena (influence of the solid melt on the boundary layers) and thus on the radial heat exchange. A comparison of the profile of the Nusselt number obtained in the present study with profiles obtained in the literature [48, 14, 22] for an immersed jet without melting showed a good agreement for low ablated depths.

This work will be completed by CFD scale simulations which will be validated on these data, first with an immersed water jet, then with a free-surface water jet [20]. The numerical simulations are in progress and will be presented, analyzed and compared to the experimental results in a forthcoming paper.

CFD simulations of immersed steel jet will also be achieved and results will be compared to the derived zero-dimensional correlation established on water to question the validity of this expression with another fluid. Studying the differences in heat transfer between immersed and free jets will also enable to make progress on this issue.

Appendix A. Evolution of Re_j and Pr_j with the temperature

Lecoanet [18] gives several laws for the evolution of the physical properties of ice and water, based on several articles [33, 9, 16]. This gives the following temperature laws for Re_j and Pr_j:

$$Re(T) \simeq \frac{996.9\cdot\left[1-3.17\cdot10^{-4}(T-298,15)-2.56\cdot10^{-6}(T-298,15)^2\right]\cdot U_jD_j}{[1+0.015512\cdot(T-293,15)]^{-1.572}\cdot10^{-3}} \quad \text{(A.1)}$$

$$Pr(T) \simeq \frac{4181.8\cdot[1+0.015512\cdot(T-293,15)]^{-1.572}}{-922.47+1839.5\left(\frac{T}{T_0}\right)-1800.7\left(\frac{T}{T_0}\right)^2+525.8\left(\frac{T}{T_0}\right)^3-73.4\left(\frac{T}{T_0}\right)^4} \quad \text{(A.2)}$$

with $T_0 = 273.15\text{K}$.

Appendix B. Evaluation of uncertainties

Appendix B.1. Jet temperature uncertainty

The jet temperature is evaluated from thermocouples in the nozzle; the uncertainty ΔT of the measurements of those thermocouples is around 2K [18].

Appendix B.2. Jet velocity uncertainty

During an experiment, a flowmeter measures the instantaneous flow rate Q (in $\text{m}^3\cdot\text{s}^{-1}$). For a cylindrical tube (such as the nozzle used in the experiments) Q is defined as:

$$Q = \frac{\pi}{4}D_j^2V_j \quad \text{(B.1)}$$

For instance, measured Q vs t (obtained for an experiment performed with $V_j = 5\,\text{m}\cdot\text{s}^{-1}$ and $T_j = 323\text{K}$) is plotted in Figure B.19, showing a scattered behavior for Q with low dispersion: the measured mean value is $Q_{av} = 8.28\cdot10^{-3}\text{m}^3\cdot\text{s}^{-1}$ and the standard deviation is $\sigma_Q = 0.14\cdot10^{-3}\text{m}^3\cdot\text{s}^{-1}$. The uncertainty on Q is taken as $\Delta Q = 2\sigma_Q$.

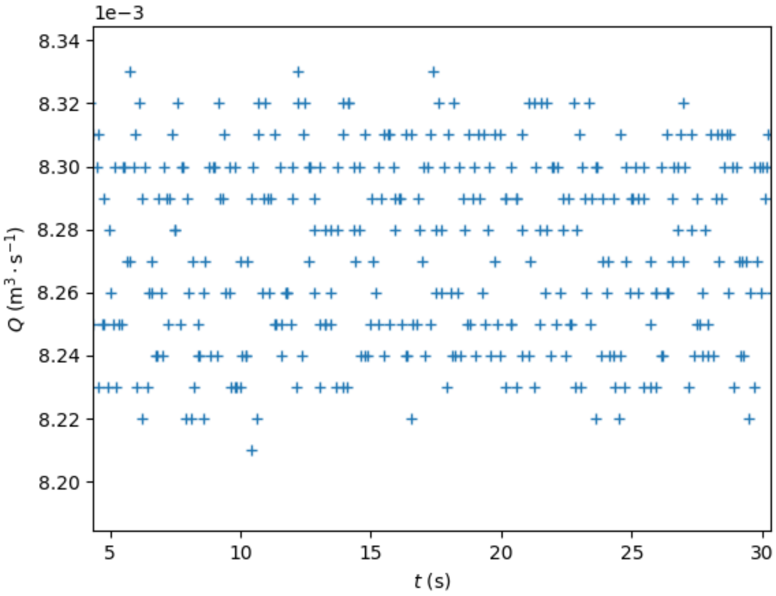

Figure B.19: Example of flowrate measurements, obtained for $V_j = 5\,\text{m}\cdot\text{s}^{-1}$ and $T_j = 323\text{K}$.

ΔD_j is estimated around 0.1mm [18].
Using Equation B.1 and these uncertainties, the extreme values of V_j are:

$$\begin{cases} V_{j,min} &= \frac{4}{\pi}\frac{Q-\Delta Q}{D_j+\Delta D_j} \\ V_{j,max} &= \frac{4}{\pi}\frac{Q+\Delta Q}{D_j-\Delta D_j} \end{cases} \quad \text{(B.2)}$$

The uncertainty on V_j is then computed as $\Delta V_j = \max\left(V_j - V_{j,min}, V_{j,max} - V_j\right)$.

Appendix B.3. Dimensionless numbers uncertainties

The uncertainties on the dimensionless numbers are obtained as follows:

- B only depends on T_j, so the extreme values B_{min} and B_{max} are computed on the range of temperature $[T_j - \Delta T_j; T_j + \Delta T_j]$. The uncertainty on B is then computed as $\Delta B = \max(B - B_{min}, B_{max} - B)$. The same method is used for Pr_j.
- ΔRe_j is computed from ΔV_j, ΔD_j and from ν_{max} and ν_{min} which are the extreme values of ν on the range of temperature $[T_j - \Delta T_j; T_j + \Delta T_j]$. The extreme values $Re_{j,max}$ and $Re_{j,min}$ are then computed as:

$$\begin{cases} Re_{j,min} & = \frac{(V_j - \Delta V_j)\cdot(D_j - \Delta D_j)}{\nu_{max}} \\ Re_{j,max} & = \frac{(V_j + \Delta V_j)\cdot(D_j + \Delta D_j)}{\nu_{min}} \end{cases} \tag{B.3}$$

Finally the uncertainty on Re_j is computed as:

$$\Delta Re_j = \max(Re_j - Re_{j,min}, Re_{j,max} - Re_j) \tag{B.4}$$

Appendix B.4. Uncertainty on the stagnation Nusselt number

The uncertainty on the stagnation ablation velocity $V_{m,0}$ (Equation (8)) is computed from the uncertainties on T_j, on D_j and on the pixel to centimeter conversion uncertainty Δ_{px}.

The pixel to centimeter conversion d_{px} (cm^{-1}) is determined before performing the experiment by putting a ruler at the location of the block and taking a picture with the high-speed camera. The distance in terms of pixel to obtain a centimeter on the picture is then measured 20 times by the user, leading to a standard deviation σ_{px} on the pixel to centimeter conversion. Δ_{px} is taken as $2\sigma_{px}$.

The dependence of $V_{m,0}$ on the parameters of the problem is unknown, thus the uncertainty $\Delta V_{m,0}$ is computed as:

$$\Delta V_{m,0} \; = \; V_{m,0}\cdot\sqrt{\left(\frac{\Delta_{px}}{d_{px}}\right)^2 + \left(\frac{\Delta T_j}{T_j}\right)^2 + \left(\frac{\Delta V_j}{V_j}\right)^2} \tag{B.5}$$

Using Equation (7), the extreme value of Nu_0 are computed as:

$$\begin{cases} Nu_{0,min} & = \min_T\left(\frac{\rho_s c_{p,j}}{\lambda_j}\right)\cdot\frac{(V_{m,0} - \Delta V_{m,0})\cdot(D_j - \Delta D_j)}{B + \Delta B} \\ Nu_{0,max} & = \max_T\left(\frac{\rho_s c_{p,j}}{\lambda_j}\right)\cdot\frac{(V_{m,0} + \Delta V_{m,0})\cdot(D_j + \Delta D_j)}{B - \Delta B} \end{cases} \tag{B.6}$$

where $\max_T$ (resp. $\min_T$) is a maximization (resp. minimization) operator on the range of temperature $[T_j - \Delta T_j; T_j + \Delta T_j]$.

Finally, the uncertainty on Nu_0 is computed as:

$$\Delta Nu_0 = \max(Nu_0 - Nu_{0,min}, Nu_{0,max} - Nu_0) \tag{B.7}$$

Appendix B.5. Uncertainty on the Reynolds number exponent α

The uncertainty on the exponent α on Re_j (in Equation 13) for a given value of T_j is evaluated by using the uncertainties on Re_j and Nu_0. α vs y_0/D_j is obtained from regressions on the points Nu_0 vs Re_j for several values of y_0/D_j.

In order to take into account the uncertainties on Nu_0 and Re_j, regressions are also performed on $Nu_0 + \Delta Nu_0$ vs $Re_j - \Delta Re_j$ (those points are noted "top" points) and on $Nu_0 - \Delta Nu_0$ vs $Re_j + \Delta Re_j$ (noted "bottom" points). Those points correspond to the extreme values of Nu_0 and Re_j.

The regressions on the top points (resp. bottom) lead to a curve $\alpha_{top,y_0/D_j}$ vs y_0/D_j (resp. $\alpha_{bottom,y_0/D_j}$ vs y_0/D_j). The curves obtained are represented as the uncertainty range in Figures 7a and 7b.

Finally, the uncertainty on the retained value of α noted here α_{av} (the average value of α on the range of depth considered) is computed as:

$$\Delta\alpha = \max\left(\max_{y_0/D_j}|\alpha_{y_0/D_j} - \alpha_{av}|, \; \max_{y_0/D_j}|\alpha_{top,y_0/D_j} - \alpha_{av}|, \; \max_{y_0/D_j}|\alpha_{bottom,y_0/D_j} - \alpha_{av}|\right) \tag{B.8}$$

which means that the maximum of the deviation from the mean value α_{av} is taken as the uncertainty $\Delta\alpha$.

References

[1] A. Bachrata, F. Bertrand, N. Marie, A. Edeline, R. Kubota, K. Kamiyama, and S. Kubo. Severe accident studies on the efficiency of mitigation devices in a sfr core with simmer code. *Nuclear Engineering and Design*, 373:111037, July 2021.

[2] P. Bakke. An experimental investigation of a wall jet. *Journal of Fluid Mechanics*, 2(05):467, July 1957.

[3] A. Bejan. *Convection Heat Transfer*. Wiley, 1 edition, April 2013.

[4] F. Bertrand, A. Bachrata, N. Marie, A. Kubo, Y. Onoda, A. Shibata, R. Kubota, and B. Carluec. Mitigation of severe accidents for sfr and associated event sequence assessment. *Nuclear Engineering and Design*, 372:110993, July 2021.

[5] J. E. Chamberlain. Heat transfer between a turbulent round jet and a segmented flat plate perpendicular to it. Master's thesis, Newark College of Engineering, 1966.

[6] K. Choo, B. K. Friedrich, A. W. Glaspell, and K. A. Schilling. The influence of nozzle-to-plate spacing on heat transfer and fluid flow of submerged jet impingement. *International Journal of Heat and Mass Transfer*, 97:66–69, June 2016.

[7] A. Dróżdż, P. Niegodajew, M. Romańczyk, and W. Elsner. Effect of Reynolds number on turbulent boundary layer approaching separation. *Experimental Thermal and Fluid Science*, 125:110377, July 2021.

[8] M. Epstein. The effect of melting on heat transfer to submerged bodies. *Letters in Heat and Mass Transfer*, 2(2):97–103, March 1975.

[9] S. Fukusako. Thermophysical properties of ice, snow, and sea ice. *International Journal of Thermophysics*, 11(2):353–372, March 1990.

[10] A. Furutani, S. Imahori, K. Sato, and M. Saito. Erosion behavior of a solid plate by a liquid jet - effect of molten layer. *Nuclear Engineering and Design*, 132(2):153–169, 1991.

[11] J. W. Gauntner, P. Hrycak, and J. N. B. Livingood. Survey of literature on flow characteristics of a single turbulent jet impinging on a flat plate. Technical report, NASA, January 1970. Number: NASA-TN-D-5652.

[12] R. R. Gilpin. The Ablation of Ice by a Water Jet. *Transactions of the Canadian Society for Mechanical Engineering*, 2(2):91–96, June 1973.

[13] M. B. Glauert. The wall jet. *Journal of Fluid Mechanics*, 1(06):625, December 1956.

[14] R. J. Goldstein and M. E. Franchett. Heat Transfer From a Flat Surface to an Oblique Impinging Jet. *Journal of Heat Transfer*, 110(1):84–90, February 1988.

[15] H. Görtler. Berechnung von Aufgaben der freien Turbulenz auf Grund eines neuen Näherungsansatzes . *ZAMM - Zeitschrift für Angewandte Mathematik und Mechanik*, 22(5):244–254, 1942.

[16] E. O. Holzbecher. *Modeling Density-Driven Flow in Porous Media*. Springer Berlin Heidelberg, Berlin, Heidelberg, 1998.

[17] K. Jambunathan, E. Lai, M. A. Moss, and B. L. Button. A review of heat transfer data for single circular jet impingement. *International Journal of Heat and Fluid Flow*, 13(2):106–115, June 1992.

[18] A. Lecoanet. *Ablation d'une paroi solide par un jet liquide*. PhD thesis, Université de Lorraine, Nancy, January 2021.

[19] A. Lecoanet, F. Payot, C. Journeau, N. Rimbert, and M. Gradeck. Classification of ablation mode during impact of hot liquid jet on a solid. *International Journal of Heat and Mass Transfer*, 181:121883, 2021.

[20] A. Lecoanet, F. Payot, C. Journeau, N. Rimbert, and M. Gradeck. Study of the ablation consecutive to jet impingement on a meltable solid – application to sfr core-catcher. *Nuclear Engineering and Design*, 377:111147, 2021.

[21] Alexandre Lecoanet, Michel Gradeck, Xiaoyang Gaus-Liu, Thomas Cron, Beatrix Fluhrer, Frédéric Payot, Christophe Journeau, and Nicolas Rimbert. Ablation of a Solid Material by High-Temperature Liquid Jet Impingement: An Application to Corium Jet Impingement on a Sodium Fast Reactor Core-Catcher. *Journal of Nuclear Engineering and Radiation Science*, 8(1):011308, January 2022.

[22] Jungho L. Lee, S. Stagnation region heat transfer of a turbulent axisymmetric jet impingement. *Experimental Heat Transfer*, 12(2):137–156, April 1999.

[23] G. Li, M. Liu, J. Wang, D. Chong, and J. Yan. Crust behavior and erosion rate prediction of EPR sacrificial material impinged by core melt jet. *Nuclear Engineering and Design*, 314:44–55, April 2017.

[24] G. Li, M. Liu, J. Wang, D. Chong, and J. Yan. Numerical study of thermal erosion behavior of RPV lower head wall impinged by molten corium jet with particle method. *International Journal of Heat and Mass Transfer*, 104:1060–1068, January 2017.

[25] J. H. Lienhard. Liquid jet impingement. *Annual Review of Heat Transfer*, 6(6):199–270, 1995.

[26] J. H. Lienhard. Heat Transfer in Flat-Plate Boundary Layers: A Correlation for Laminar, Transitional, and Turbulent Flow. *Journal of Heat Transfer*, 142(6):061805, June 2020.

[27] X. Liu, J. H. Lienhard, and J. S. Lombara. Convective Heat Transfer by Impingement of Circular Liquid Jets. *Journal of Heat Transfer*, 113(3):571–582, August 1991.

[28] J. N. B. Livingood and P. Hrycak. Impingement heat transfer from turbulent air jets to flat plates: A literature survey. Technical Report NASA-TM-X-2778, NASA, May 1973. NTRS Author Affiliations: NASA Lewis Research Center, Newark Coll. of Engr. NTRS Document ID: 19730016200 NTRS Research Center: Legacy CDMS (CDMS).

[29] A. S. Lopes, U. Piomelli, and J. M. L. M. Palma. Large-eddy simulation of the flow in an S-duct. *Journal of Turbulence*, 7:N11, January 2006.

[30] N. Machicoane, J. Bonaventure, and R. Volk. Melting dynamics of large ice balls in a turbulent swirling flow Melting dynamics of large ice balls in a turbulent swirling flow. *Physics of Fluids*, 25, 2013.

[31] H. Martin. Heat and Mass Transfer between Impinging Gas Jets and Solid Surfaces. In *Advances in Heat Transfer*, volume 13, pages 1–60. Elsevier, 1977.

[32] G. E. A. Meier. *Active Control of Boundary Layer and Separation*, pages 203–233. Springer Vienna, Vienna, 1996.

[33] P. Mouchet and M. Roustan. Caractéristiques et propriétés des eaux - Eau pure, eaux naturelles. *Technologies de l'eau*, February 2011.

[34] S. B. Pope. *Turbulent flows.* Cambridge University Press, Cambridge ; New York, 2000.

[35] N. Rajaratnam. *Turbulent Jets.* Elsevier, Burlington, 1976. OCLC: 476237941.

[36] K. Sato, A. Furutani, M. Saito, M. Isozaki, K. Suganuma, and S. Imahori. Melting attack of solid plates by a high-temperature liquid jet [II] — Erosion behavior by a molten metal jet. *Nuclear Engineering and Design*, 132(2):171–186, December 1991.

[37] H. Schlichting and K. Gersten. *Boundary-Layer Theory.* Springer Berlin Heidelberg, Berlin, Heidelberg, 2017.

[38] A. Sigalla. Measurements of Skin Friction in a Plane Turbulent Wall Jet. *The Journal of the Royal Aeronautical Society*, 62(576):873–877, December 1958.

[39] V. A. Smirnov, G. E. Verevochkin, and P. M. Brdlick. Heat transfer between a jet and a held plate normal to flow. *International Journal of Heat and Mass Transfer*, 2(1-2):1–7, March 1961.

[40] M. J. Swedish, M. Epstein, J. H. Linehan, G. A. Lambert, G. M. Hauser, and L. J. Stachyra. Surface ablation in the impingement region of a liquid jet. *AIChE Journal*, 25(4):630–638, July 1979.

[41] J. Taghinia, M. Rahman, and T. Siikonen. Heat transfer and flow analysis of jet impingement on concave surfaces. *Applied Thermal Engineering*, 84:448–459, June 2015.

[42] I. Tani and Y. Komatsu. Impingement of a round jet on a flat surface. In Henry Görtler, editor, *Applied Mechanics*, pages 672–676, Berlin, Heidelberg, 1966. Springer Berlin Heidelberg.

[43] C. Tien and Y. Yen. The effect of melting on forced convection heat transfer. *Journal of Applied Meteorology and Climatology*, 4(4):523 – 527, 1965.

[44] W. Tollmien. Calculation of Turbulent Expansion Processes. Technical report, NACA, September 1945. Number: NACA-TM-1085.

[45] W. Tromm and X. Gaus-Liu. Kit-jimec experiments to investigate jet impingement on the ablation of core catcher bottom. In *NENE International Conference Nuclear Energy for New Europe*, 6-9 sep. 2021.

[46] R. Viskanta. Heat transfer to impinging isothermal gas and flame jets. *Experimental Thermal and Fluid Science*, 6(2):111–134, February 1993.

[47] B. W. Webb and C. F. Ma. Single-phase liquid jet impingement heat transfer. *Advances in heat transfer*, 26:105–217, 1995.

[48] J. Wienand, A. Riedelsheimer, and B. Weigand. Numerical study of a turbulent impinging jet for different jet-to-plate distances using two-equation turbulence models. In *16th International Symposium on Transport Phenomena and Dynamics of Rotating Machinery*, Honolulu, United States, April 2016.

[49] S. Yoshioka and P. H. Alfredsson. Control Of Turbulent Boundary Layers By Uniform Wall Suction And Blowing. In Rama Govindarajan, editor, *IUTAM Symposium on Laminar-Turbulent Transition*, volume 78, pages 437–442, Dordrecht, 2006. Kluwer Academic Publishers. Series Title: Fluid Mechanics and Its Applications.